CORE
Metadata, citation and similar papers at core.ac.uk
Provided by IntechOpen

We are IntechOpen, the world's leading publisher of Open Access books Built by scientists, for scientists

4,800
Open access books available

122,000
International authors and editors

135M
Downloads

Our authors are among the

154
Countries delivered to

TOP 1%
most cited scientists

12.2%
Contributors from top 500 universities

WEB OF SCIENCE™

Selection of our books indexed in the Book Citation Index in Web of Science™ Core Collection (BKCI)

Interested in publishing with us?
Contact book.department@intechopen.com

Numbers displayed above are based on latest data collected.
For more information visit www.intechopen.com

10

Symmetry and Lattice Dynamics

Hui Tang[1], Bing-Shen Wang[2] and Zhao-Bin Su[3]
[1]*Institute of Physics, Chinese Academy of Sciences*
[2]*Institute of Semiconductors, Chinese Academy of Sciences*
[3]*Institute of Theoretical Physics, Chinese Academy of Sciences*
China

1. Introduction

Hexagon is one of the most beautiful substance structures in nature. From snowflakes to honeycomb lattices, we can find the presence and stability of this delicate structure. The two-dimensional hexagon had been investigated in graphite materials which has an evident layered structure (Painter & Ellis, 1970) long before the discovery of graphene. Since the successful fabrication of graphene (Berger et al., 2004; Novoselov et al., 2004), a monolayer of carbon atoms tightly packed into a two-dimensional hexagonal lattice, its various properties have been widely explored and have received increasing attention (Castro Neto et al., 2009; Das et al., 2008; Ferrari et al., 2006; Gupta et al., 2006; Partoens & Peeters, 2006; 2007). Its exotic electronic property has the potential for practical applications and provides a prospect of theoretical invention. On the other hand, graphene is a basic structural element of many carbon allotropes including graphite, charcoal, carbon nanotubes and fullerenes. It is also of theoretical significance and practical guidance to study the physical properties such as the lattice dynamics and electronic structures starting from graphene and extending to other related systems.

It is well known that symmetry concept plays an important role in physics. Specifically, in condensed matter physics, the microscopic symmetry of the structures of materials determines the symmetry properties of macroscopic physical quantities. Group theory is not only a powerful tool to classify the electronic and phonon spectra, but also essential to understand the inherent physical meaning as well as their consequence. The symmetry group D_{6h} of graphene is the basic building block of all carbon allotropes in a sense that either their symmetry groups evolve from D_{6h} with a few symmetry operations lifted or added, or some symmetry operations in D_{6h} are inherited in a certain forms. The study of symmetry provides an effective way to find the common essence and differences among carbon allotropes. In this chapter we will analyze the symmetry characteristics as well as symmetry induced constrains to the lattice dynamics of graphene, multilayered graphene, and nanotubes.

Lattice dynamics studies the vibration of lattice, i.e. the phonons. Many exotic properties of graphene, such as its very high strength and thermal conductivity are directly connected to the phonon properties. Its extremely high electrical conductivity is also related to the phonon dispersion and electron-phonon interactions. We will focus on the lattice dynamics of the multilayered graphene systems, where graphene is the limit of one layer number, and the nanotube systems with different radius and charity. In particular, the role of

symmetry selection in optical activeness of phonon modes in multilayer graphene systems and symmetry restriction in the phonon dispersion calculation of carbon nanotubes is emphasized.

Multilayered graphene systems can be viewed as stacking a few number of graphene layers along the direction perpendicular to planar sheets. Some symmetry operations existed in graphene such as the space reflection $\hat{\sigma}_i$ or reflection with the plane $\hat{\sigma}_h$ may lift depending on the arrangement of layers and the layer number. The breaking of the symmetry operations reduces the order of symmetry groups and causes the change of the optical activities of the phonon branches. Quantitatively, the phonon modes will be softer or harder (red or blue shift) as the number of layers changed. All these qualitative and quantitative properties will be discussed in the next two sections and calculated results are compared with the experimental measurements.

Carbon nanotubes had been discovered (Iijima, 1991) before the fabrication of graphene. At first sight, nanotubes and graphene belong to totally different symmetry groups and follow the different symmetry restrictions on their physical properties. In virtue of the picture that a single wall carbon nanotube can be viewed as a warped graphene stripe (Saito et al., 1998), we still can ask what is the effect of the added periodic edge condition on the two sides of the stripe, and what is the consequence of the three-fold rotational $\hat{C}_3$ symmetry on graphene. In section 4, we will reveal a three-theta role, an universal triple chiral angle (3θ) dependence, of nanotubes with different chiral angles, which is actually the heritage of the three-fold rotational symmetry of graphene.

As usual, the enlargement of the primitive cell in real lattice space causes Brillouin zone folding in reciprocal space. If the edge effects of stripes and the curvature effects of nanotubes are neglected, the electronic dispersions in new small Brillouin zone can be obtained directly by folding those of graphene. For phonons, the situation would be more complicated because of their vector properties. Particularly, flexure modes (a kind of vibrational modes with parabolic dispersions when surface exists (Mahan & Jeon, 2004)) can be obtained only when a correct form of the potential energy satisfying the symmetry constrains is adopted. The emergence of the twist mode is intimately connected with the geometrical structure of the rod-like cylindrical systems.

The one-dimensional (1D) single wall carbon nanotubes belong to 1D line groups (Damnjanović et al., 1999; 2000). For chiral nanotubes, the definition of the primary chiral operation is not unique. This will result in different choice of primitive cells and the different coordinates in description of the lattice structure of nanotubes. There are two commonly used coordinates for nanotubes, thus two sets of good quantum numbers. One of them will be called it Dresselhaus coordinate (Saito et al., 1998), which has the superiority in denoting the optical transition properties at long wave length limit. The other is White coordinate (Gunlycke et al., 2008; White et al., 1993), which has a clear relation with the symmetry generators. Since the quantum numbers in Dresselhaus coordinate are related to an isogonal group of the symmetry group of the nanotube, the relation between these two sets of quantum numbers is not trivial and we will discuss it in detail in section 5. With this relation, it is easy to transform electronic or phonon dispersions with one set of good quantum numbers to the others. Finally, to illustrate the similarities and differences among carbon allotropes, the lattice dynamics of single-wall carbon nanotubes is discussed in section 6.

2. The symmetry consideration in graphene and multilayer graphene systems

Graphene is a monolayer carbon atoms with the hexagonal lattice configuration which is characterized by the D_{6h} symmetry. There are two identical carbon atoms in one unit cell as shown in Fig. 1, and the bond length between two nearest-neighbor atoms in the plane is $b = 1.42$ Å(Saito et al., 1998). The primitive lattice vectors can be set as $\vec{a}_1$ and $\vec{a}_2$ with $|\vec{a}_1| = |\vec{a}_2| = 2.46$ Å. The lattice configuration of multilayer graphene systems (MLGS) is constructed by stacking N graphene sheets along perpendicular direction, z axis. The distance between two adjacent layers is about $\frac{c}{2} = 3.35$ Å which is much larger than the in-plane bond length (Manes et al., 2007). AA-stacked or AB-stacked MLGS can be obtained respectively if all layers have the same configuration or shift alternately along one of the first-nearest carbon-carbon bonds in horizontal plane as shown in Fig. 2. The three-dimensional (3D) graphite is the limitation of AB-stacked MLGS with layer number $N \to \infty$.

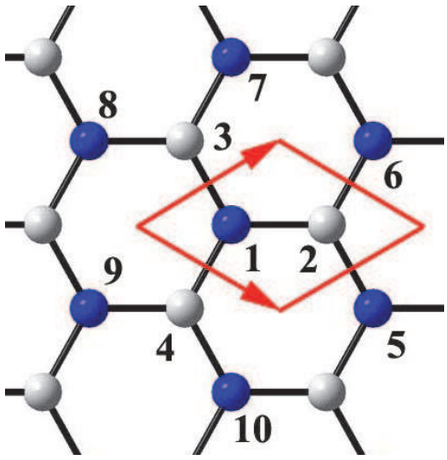

Fig. 1. The sketch of the lattice configuration of graphene. The vectors shown in the figure are the primitive lattice vectors $\vec{a}_1$ and $\vec{a}_2$.

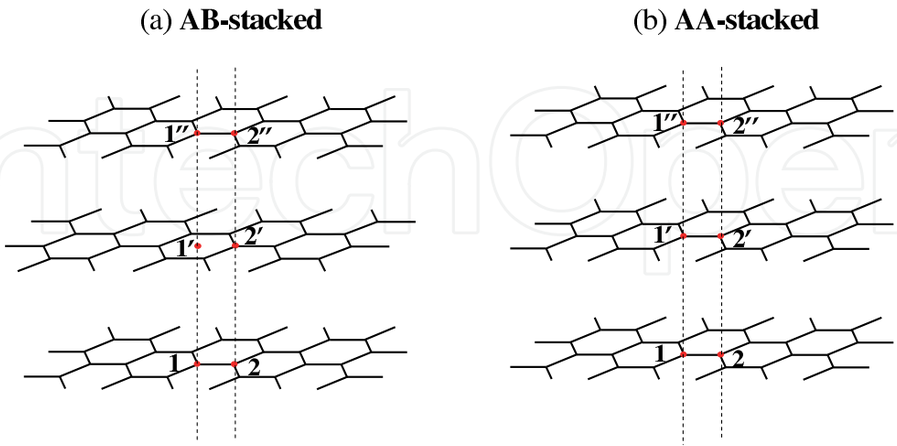

Fig. 2. The sketch of the configurations of AB-stacked in (a) and AA-stacked in (b) for multilayer graphene.

There are twelve conjugacy classes in D_{6h} group and thus twelve irreducible representations. For simplifying the discussion, D_{6h} can be expressed as the direct products of three subgroups,

$$D_{6h} = D_3 \otimes \{\hat{E}, \hat{\sigma}_h\} \otimes \{\hat{E}, \hat{\sigma}_i\} ,$$
$$D_3 = \{\hat{E}, 2\hat{C}_3, 3\hat{C}_2\} ,$$

where $\hat{\sigma}_h$ is the reflection with the plane, $\hat{\sigma}_i$ the space reflection, $\hat{C}_3$ three-fold rotation around the axis perpendicular to the graphene sheet, and $\hat{C}_2$ two-fold rotation around axis parallel to the sheet. There are three irreducible representations for D_3 group, two one-dimensional representations A and B and one two-dimensional representation E. The twelve irreducible representations of D_{6h} can be denoted by A, B, and E with the subscripts $1, 2$ and u, g, where letters are for representations of D_3, and the subscripts correspond to the parity under $\hat{\sigma}_h$ and $\hat{\sigma}_i$ respectively. The symbol for the irreducible representations we used here is the notation used in Ref. (Eyring et al., 1949) which is most commonly used in the treatment of molecules. For AB-stacked MLGS, the symmetry operations $\hat{\sigma}_h$ and $\hat{\sigma}_i$ existed in graphene cannot coexist anymore, and the point groups will depend on the layer number (Manes et al., 2007). For AB-stacked even number MLGS (EMLGS), the space reflection $\hat{\sigma}_i$ exists with respect to the middle point of pair atoms 2′ in the $\frac{N}{2}$-th layer and 1″ in the $\frac{N}{2}+1$-th layer as shown in Fig. 2(a). But there is no planar reflection $\hat{\sigma}_h$. Same as that in graphene, the two $\hat{C}_3$ and three $\hat{C}_2$ operations exist. The three two-fold axes are perpendicular to z axis with angle $\pi/3$ between each other. All the symmetry operations constitute the point group $D_{3d} = D_3 \otimes \{\hat{E}, \hat{\sigma}_i\}$. In AB-stacked odd number MLGS (OMLGS), the space reflection $\hat{\sigma}_i$ is lift instead of $\hat{\sigma}_h$ in EMLGS. The reference plane of $\hat{\sigma}_h$ is set at the middle layer of OMLGS as shown in Fig. 2(b). All operations of D_3 also exist, but the three 2-fold axes are one to one perpendicular to those of $\hat{C}_2$ in EMLGS. Consequently, the symmetry group of OMLGS is $D_{3h} = D_3 \otimes \{\hat{E}, \hat{\sigma}_h\}$.

The point group of the 3D graphite is the non-symmorphic group D^4_{6h} with non-primitive translation $\vec{\tau} = \frac{1}{2}\vec{c}$ (Brillson et al., 1971). In addition to the in-plane translation symmetry, there exists translation symmetry along z for the 3D graphite. The primitive vector along z is set as $\vec{c}$ which crosses the two adjacent layers. Thus there are four carbon atoms 1, 2, 1′, and 2′ in one unit cell as represented in Fig. 2(a).

As described in Ref. (Jiang et al., 2008, a), the environment of an atom in graphite or AB-stacked MLGS is more complicated than that in 2D graphene. The in-layer situation is the same as that of graphene, i.e. three nearest-neighbor carbon atoms and six next-nearest-neighbors for any one of carbon atom. For the inter-layer atomic positions, picking atom 2′ in the middle layer of Fig. 2(a) as an example, there are two inter-layer nearest-neighbor atoms 2 and 2″ in each of the two adjacent layers with the distance $c/2$ respectively. Furthermore, there are three inter-layer next-nearest-neighbor atoms around atom 2′ with distance $\sqrt{b^2 + (c/2)^2}$ in one of the adjacent layer (such as atom 1 is one of them). The adjacent environment of atom 1 is quite different from that of atom 2′. Because the position 1′ in Fig. 2(a) has no atom, atom 1 has no inter-layer nearest-neighbors. Instead it has six inter-layer next-nearest-neighbors in one of the adjacent layer with the same distance $\sqrt{b^2 + (c/2)^2}$.

In the AA-stacked MLGS as well as the AA-stacked 3D graphite, all layers have the same configuration. So that all of them have the same point group D_{6h} as that in graphene whatever the layer number is even or odd. Different from the graphite (AB-stacked 3D graphite), there are only two atoms in the unit cell and the primitive translation along z axis is $\vec{c}/2$ for AA-stacked 3D graphite. As shown in Fig. 2(b), the environment of a carbon atom in

the AA-stacked MLGS is simpler than that in AB-stacked MLGS. For each atom, there are one inter-layer nearest-neighbors in one of the adjacent layer with the distance $c/2$ and three inter-layer second-nearest-neighbors with distance $\sqrt{b^2+(c/2)^2}$.
Taking the lattice displacements $\vec{u}_i$ (i runs over all atoms in one unit cell) as bases, the dynamical representation Γ^{dyn} can be expressed as the direct products of the vector representation Γ^v and atomic permutation representation Γ^{atom} for a given group, $\Gamma^{dyn} = \Gamma^v \otimes \Gamma^{atom}$. By applying the projection operator technique, the dynamical representation Γ^{dyn} is decomposed into the irreducible representations of the corresponding groups of graphene, MLGS with N even and odd, and 3D graphite respectively. Referring to Ref. (Elliott & Dawber, 1979), the infra-red (Ir) active phonon modes should be compatible with the same decomposed irreducible representations as the vector representation Γ^v, while the Raman active phonon modes correspond to the same irreducible representations shown up in the decomposition of a six-dimension representation with d-wave like bases: x^2+y^2, z^2, x^2-y^2, xy, yz, and zx. The three acoustic modes with zero frequency at the Γ point, which correspond to the vector representation Γ^v, are excluded in the consideration of Ir and Raman active modes.

	Group	Γ^{dyn}	Γ^{Ir}	Γ^{R}
graphene[a]	D_{6h}	$A_{2u} \oplus B_{2g} \oplus E_{1u} \oplus E_{2g}$	/	E_{2g}
AB-stacked	D_{3d} [b]	$N(A_{1g} \oplus A_{2u} \oplus E_g \oplus E_u)$	$(N-1)A_{2u} \oplus (N-1)E_u$	$NA_{1g} \oplus NE_g$
	D_{3h} [b]	$(N-1)A_{1g} \oplus (N+1)A_{2u}$ $\oplus (N+1)E_g \oplus (N-1)E_u$	$NA_{2u} \oplus NE_g$	$(N-1)A_{1g}$ $\oplus NE_g \oplus (N-1)E_u$
	D_{6h}^4 [c]	$2(A_{2u} \oplus B_{2g} \oplus E_{1u} \oplus E_{2g})$	$A_{2u} \oplus E_{1u}$	$2E_{2g}$
AA-stacked	D_{6h} (even)	$\frac{N}{2}(A_{1g} \oplus A_{2u} \oplus B_{1u} \oplus B_{2g} \oplus E_{1u}$ $\oplus E_{1g} \oplus E_{2g} \oplus E_{2u})$	$(\frac{N}{2}-1)(A_{2u} \oplus E_{1u})$	$\frac{N}{2}(A_{1g} \oplus E_{1g} \oplus E_{2g})$
	D_{6h} (odd)	$\frac{N-1}{2}(A_{1g} \oplus B_{1u} \oplus E_{1g} \oplus E_{2u})$ $\oplus \frac{N+1}{2}(A_{2u} \oplus B_{2g} \oplus E_{1u} \oplus E_{2g})$	$\frac{N-1}{2}(A_{2u} \oplus E_{1u})$	$\frac{N-1}{2}(A_{1g} \oplus E_{1g})$ $\oplus \frac{N+1}{2}E_{2g}$
	D_{6h}	$A_{2u} \oplus B_{2g} \oplus E_{1u} \oplus E_{2g}$	/	E_{2g}

Table 1. The symmetry analysis of the phonon modes at the center point of Brillouin zone for AA- or AB-stacked MLGS. Phonon modes are classified by the decomposition of Γ^{dyn} . The irreducible representations of the Ir and Raman active modes are also listed.
[a]Reference (Saito et al., 1998); [b]Reference (Manes et al., 2007); [c]Reference (Mani et al., 1974).

We show in Table 1 the symmetry analysis (Jiang et al., 2008, a) of phonon modes and the Raman active and Ir active modes for graphene, AB- and AA-stacked MLGS, and 3D graphite. Two straightforward consequences can be find out for the Ir and Raman active modes in AB-stacked MLGS. Firstly, in the EMLGS with D_{3d} point group, as well as in graphene and 3D graphite, phonon modes cannot be Ir and Raman active simultaneously. However, in the OMLGS with D_{3h} point group, the N E_g modes are both Ir and Raman active. This is because there is no inversion center in the OMLGS. Secondly, an optical mode (denoted as the inter-layer optical mode) belongs to the A_{1g} representation with Raman active in the EMLGS (D_{3d}) and A_{2u} Ir active in the OMLGS (D_{3h}). This mode can be further identified as vibrational displacements perpendicular to the constituent layers, and oscillating with each layer as a whole but alternatively from layer to layer. These properties can be used as criterion to identify the layer number being even or odd for AB-stacked MLGS.
In the AA-stacked MLGS with N either even or odd, the symmetry group is D_{6h} which includes both σ_i and σ_h. Consequently, no phonon modes would be Ir and Raman active simultaneously in AA-stacked MLGS. Interestingly, the inter-layer optical mode mentioned above belongs to the different representations so that different active for even and odd layer numbers. In detail, it belongs to A_{1g} Raman active in the EMLGS and A_{2u} Ir active in the

OMLGS, which is the same as that in AB-stacked MLGS. Due to its vibration direction, the inter-layer optical mode favors to take the maximum advantage of the inter-layer interactions. From the next section, it is known that this optical mode would be the most sensitive mode to the layer numbers in a few layer systems and becomes a useful candidate in experiments to identify the even-oddness of the MLGS and the layer numbers.

3. Lattice dynamics of multilayer graphene systems

3.1 Vibrational potential energy

For providing a simple and straightforward method to relate the phonon modes with atomic movement modality, we choose an semi-phenomenological model of vibrational potential energy (Aizawa et al., 1990; Aizawa, 1991; Jiang et al., 2008, a) to study the lattice dynamics of graphene and multilayer graphene systems (MLGS). The lattice vibration energy in this model is expressed in quadratic terms of lattice displacements. So that it is easy to check term by term the symmetric invariance, such as the translational invariance and rigid rotational invariance, which are the essential restrictions to derive the correct phonon modes. Besides, because the potential energy is one of the key aspects in determine the vibration properties, it is possible to use the same potential terms of graphene into in-layer case of MLGS and even to carbon nanotubes, which will be discussed in more detailed in section 6.

We begin from the one graphene layer, where the vibrational potential energy can be described by five quadratic terms (Aizawa et al., 1990; Aizawa, 1991). They are the first and second nearest-neighbor radical spring stretching, the in-plane bond angle variations, the out-of-surface bond bending, and the bond twisting energies. The detailed expressions of five terms, taking atom 1 in Fig. 1 as an example, are listed in the following.

(1) V_l is the potential of the radical spring force between the nearest-neighbor atom pair,

$$V_l = \frac{k_l}{2} \sum_{i=2}^{4} [(\vec{u}_i - \vec{u}_1) \cdot \vec{e}^{\,l}_{1i}]^2 \,, \tag{1}$$

where k_l is the first-order force constant and $\vec{e}^{\,l}_{1i} = \frac{\vec{r}_{1i}}{|\vec{r}_{1i}|}$.

(2) V_{sl} is similar to the first term but between a pair of next nearest-neighbored atoms illustrated as $(1, 5 \ldots 10)$ in Fig. 1,

$$V_{sl} = \frac{k_{sl}}{2} \sum_{i=5}^{10} [(\vec{u}_i - \vec{u}_1) \cdot \vec{e}^{\,l}_{1i}]^2 \tag{2}$$

with k_{sl} the second-order force constant.

(3) The potential energy for the in-plane bond bending V_{BB} is actually a term associated with bond angle variations. Three atoms are involved:

$$\begin{aligned} V_{BB} &= \frac{k_{BB}}{4} \sum_{j_i} \sum_{\substack{j'_i \\ (j'_i \neq j_i)}} \left[\frac{\vec{u}_{j_i} - \vec{u}_i}{r_{ij_i}} \cdot (\vec{e}^{\,l}_{ij'_i} - \cos\theta_0 \vec{e}^{\,l}_{ij_i}) + \frac{\vec{u}_{j'_i} - \vec{u}_i}{r_{ij'}} \cdot (\vec{e}^{\,l}_{ij_i} - \cos\theta_0 \vec{e}^{\,l}_{ij'_i}) \right]^2 \\ &= \frac{k_{BB}}{4} \sum_{j_i} \sum_{\substack{j'_i \\ (j'_i \neq j_i)}} (\cos\theta'_{j_i i j'_i} - \cos\theta_0)^2 \,. \end{aligned} \tag{3}$$

As i is 1 (or 2), (j_i, j_i') take the sites (2, 3), (3, 4), and (4, 2) (or (1, 5), (5, 6), and (6, 1)) respectively as shown in Fig. 1. In Eq. (3), $\theta_0 = 120^\circ$ stands for the equilibrium angle, while $\theta'_{j_i i j_i'}$ for angle in vibration between the bonds $\vec{r}_{ij_i}$ and $\vec{r}_{ij_i'}$. The expression in terms of $\vec{u}_{j_i} - \vec{u}_i$ and $\vec{u}_{j_i'} - \vec{u}_i$ is exactly same as that of $\cos\theta'$.
(4) The potential of the out-of-plane bond bending V_{rc} describes a kind of withdrawn energy of atom i by its three nearest-neighbor atoms j_i. It contains four atoms simultaneously,

$$V_{rc} = \frac{k_{rc}}{2}[(3\vec{u}_i - \sum_{j_i}\vec{u}_{j_i}) \cdot \vec{e}_z]^2, \tag{4}$$

Where i takes 1 or 2 with j_i running over the three nearest neighbors of atom i. This potential has the physical intuition as that responsible for the perpendicular optical mode and is trying to keep the four atoms on the plane.
(5) The twist potential energy for bond $\vec{r}_{1k}$ is

$$V_{tw} = \frac{k_{tw}}{2}\sum_{\langle i,j\rangle}[(\vec{u}_i - \vec{u}_j - (\vec{u}_{i'} - \vec{u}_{j'})) \cdot \vec{e}_z]^2 \ , \tag{5}$$

where $\langle i, j\rangle$ represents a pair of atoms nearest-neighbored with atom 1 while k the third of its nearest neighbors. Pair $\langle i', j'\rangle$ is for a pair of atoms nearest-neighbored with atom k. It has the intuition that responsible for modes with twisted vibrations.
From the modality of atomic movements, we can classify the above in-plane vibrational potential terms into three types and extend them to the inter-layer case (Jiang et al., 2008, a). The first type is for radical stretching movements between the two atoms located in the adjacent layers. The second describes the relative movement between the two pairs of atoms with a common one as an apex. It is evolved from the above bond bending term and three atoms form one bond in a layer and another connecting the two nearest layers. The third type is new for simulating the twist force affected on the inter-layer "bond" as shown in the sketch 3, which involves more than three atoms according to the specific bond configurations. The whole of these terms is actually a generalized valence force model to including far away atoms in response to the bond charge effect (Jeon and Mahan, 2005) in certain extent. Because the inter-layer "bond" is much longer than the in-plane bond, it is resulted that all inter-layer interactions are one or two orders less than their counterparts in layer, but they themselves have comparable contributions. We give out the inter-layer terms for the AB-stacked MLGS in the following and they can be similarly generalized to the AA-stacked MLGS.

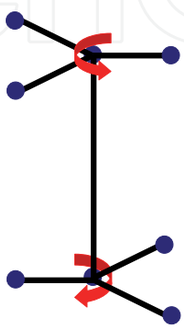

Fig. 3. The sketch of the twist force for a "bond" connecting the two adjacent layers.

(1) The inter-layer "bond" stretching energies $V_l^{(int)}$ (or $V_{sl}^{(int)}$):

$$\sum_{i,j} \frac{k'_l}{2}[(\vec{u}_i - \vec{u}_j) \cdot \vec{e}_{ij}^{\,l}]^2, \tag{6}$$

where $\vec{u}_i(\vec{u}_j)$ is the displacement vector of the atom $i(j)$ and $\vec{e}_{ij}^{\,l}$ is the unit vector from atom i to atom j. If the summation is taken over the nearest-neighbored inter-layer pair of atoms, the corresponding force constant is denoted as k'_l, while k'_{sl} for the next nearest-neighbor inter-layer pairs.
(2) For the three atoms 2, 2′ and i, where i is the in-plane nearest neighbor of atom 2 (atom 1 is one of them as shown in Fig. 2), we found by practice that under a specific configuration with atom i rather than atom 2 as an apex, a correlation term k'_{rr} has the most sensitive contribution to the layer dependence of the optical modes,

$$\frac{k'_{rr}}{2} \sum_i [(\vec{u}_2 - \vec{u}_i) \cdot \vec{e}_{i2}^{\,l} - (\vec{u}_{2'} - \vec{u}_i) \cdot \vec{e}_{i2'}^{\,l}]^2.$$

Actually the two square terms in above modality have already been accounted in the in-plane and inter-plane stretching terms respectively. Only the across term

$$V_{rr} = -k'_{rr} \sum_i [(\vec{u}_2 - \vec{u}_i) \cdot \vec{e}_{i2}^{\,l}][(\vec{u}_{2'} - \vec{u}_i) \cdot \vec{e}_{i2'}^{\,l}] \tag{7}$$

plays a real role, which weakens the interaction between the two adjacent layers. The positive definite condition for getting real frequencies is $k'_{sl} \geq k'_{rr}$.
(3) The twisting potential for an inter-layer bond between atoms 2 and 2′ is coming from the two sets of three nearest-neighbors of atoms 2 and 2′ respectively. It can be described as

$$V_{tw} = \frac{k'_{tw}}{2}[\sum_i (\vec{u}_i - \vec{u}_2) \cdot \vec{e}_i^{\,\theta} - \sum_j (\vec{u}_j - \vec{u}_{2'}) \cdot \vec{e}_j^{\,\theta}]^2, \tag{8}$$

where $\sum_i$ and $\sum_j$ represent the summation over the three in-plane first-nearest-neighbors for atoms 2 and 2′ respectively. $\vec{e}_i^{\,\theta} = \vec{e}_z \times \vec{e}_{2i}^{\,l}$ is the tangential unit vector in the plane formed by three nearest-neighbor atoms. The quadratic form as a whole ensures a proper definition for the torsion angle. For pure rotations around the bond, this expression gives zero torsion consistently. In contrast, the bond is most severely twisted when the three neighbors around atom 2 and those of atom 2′ rotate reversely.
By comparing the k'_{rr} term with V_{b-b} term (Jeon and Mahan, 2005) originated from the bond-charge model, a common point can be found that both terms have the same negative cross term. In addition, from the calculation results shown in the next subsection, two quite different frequency values in long wave length limit can be obtained to distinguish clearly the in-plane vibration and vibration along z axis. These provide an evidence that the polarization effect of graphitic materials (Saito et al., 1998) can be properly described by our vibration potential model. It can also be checked one by one that all above nine vibrational potential energy terms satisfy the rigid rotational symmetry constrain(Jiang et al., 2006; Mahan & Jeon, 2004; Popov et al., 2000) which guarantees the existence of the flexure modes with correct parabolic dispersion in low-frequency limit in low-dimensional systems. Details will be discussed in the next subsection.

3.2 Results and discussions

Because the microscopic environment of a carbon atom is almost the same in graphene, the in-layer of MLGS, and carbon nanotubes, the five intra-layer force constants we used in the following are taken from Ref. (Jiang et al., 2008, b) as $k_l = 305$ N m^{-1}, $k_{sl} = 68.25$ N m^{-1}, $k_{BB} = 1.38 \times 10^{-11}$ erg, $k_{rc} = 14.8$ N m^{-1}, $k_{tw} = 6.24$ N m^{-1}. They are originally taken references from a force-constant model for monolayer graphite formed on surfaces (Aizawa et al., 1990; Aizawa, 1991). The four inter-layer force constants are adjusted to fit the experimental values of four modes in 3D graphite as shown in Table 2. The fitting error for phonon modes is kept less than 7%. The inter-layer force constants are $k'_l = 0.77$ Nm^{-1}, $k'_{sl} = 0.95$ Nm^{-1}, $k'_{tw} = 0.64$ Nm^{-1}, $k'_{rr} = 0.9$ Nm^{-1}.

Reps	$A_1^{'}$	E_{2g}	A_{2u}	E_{2g}
Experiments	30^a	40^a	868^b	1586^b
Theory	30.2	42.7	869.9	1586.6

Table 2. Comparison of several mode frequencies (in the unit of cm^{-1}) for the AB-stacked 3D graphite between our calculating results and the experimental values: ^{a}Ref. (Nicklow et al., 1972), ^{b}Ref. (Maultzsch et al., 2004).

The phonon dispersions for the AB-stacked graphite are calculated (Jiang et al., 2008, a) according to the vibration potential energy discussed in the above subsection and shown in Fig. 4. The theoretical calculations meet the experimental results not only in the low frequency region (Nicklow et al., 1972), but also in the high frequency region (Maultzsch et al., 2004; Mohr et al., 2007). The good consistency with the experimental data shows that the vibrational potential energies and parameters are reasonable and applicable. In the figure, Γ, K, M and A points are the standard notations for the specific symmetric points in the Brillouin zone hexagonal reciprocal lattice.

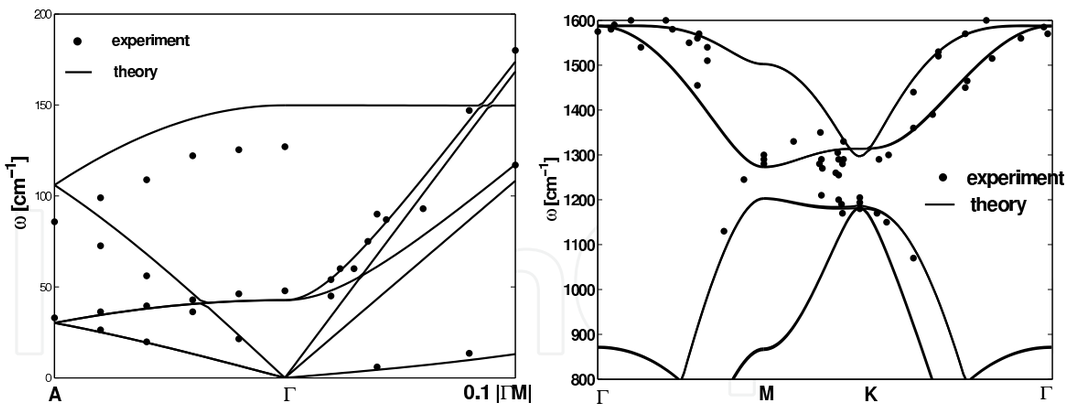

(a) The low-frequency region (b) The high-frequency region

Fig. 4. Phonon dispersion for the 3D graphite for the low-frequency region (a), and the high-frequency region (b). Solid dots are the experimental results of Ref. (Nicklow et al., 1972) in (a), and Ref. (Maultzsch et al., 2004; Mohr et al., 2007) in (b). Lines are the theoretical calculations. In Ref. (Maultzsch et al., 2004; Mohr et al., 2007), those phonon wave vectors, which were not exactly along the Γ-M or Γ-K-M direction, were projected onto the closest high-symmetry direction.

The phonon dispersions of graphene and AA-stacked 3D graphite are further calculated as shown in Fig. 5. Since the unit cell in both cases contains only two atoms in contrast to that of the AB-stacked graphite, there are six branches of phonon dispersion. Focus on the Γ point, a long wave length limit, we would mainly discuss three kinds of optical modes whose atomic movement modalities are sketched in Fig. 6. (1) The optical C-C in-plane stretching modes shown in Fig. 6(a) exist at about 1580 cm^{-1} for all three cases of graphene, AB-, and AA-stacked 3D graphite. These modes are doubly degenerated and Raman active with E_{2g} irreducible representation. Additional two degenerate optical in-plane modes very near them, which are Infra-red active belonging to E_{1u}, exist only in AB-stacked 3D graphite because it has four atoms in the unit cell. (2) An out-of-plane optical mode shown in Fig. 6(b) exists at about 860 cm^{-1} for graphene and AA-stacked 3D graphite, as well as for AB-stacked 3D graphite but double degenerated. The obvious difference between 1580 cm^{-1} mode and 860 cm^{-1} mode comes from the polarization effect of graphitic materials (Saito et al., 1998). (3) Except graphene, there exists an inter-layer optical mode shown in Fig. 6(c) for layer number equal to or greater than 2. Noticed that this mode exists at A point instead of Γ point for AA-stacked 3D graphite due to a phase factor difference of π needed between two adjacent layers. Asymptotic frequency of inter-layer optical mode in large number N is 150 cm^{-1} or 134 cm^{-1} for AB- or AA-stacked MLGS, respectively.

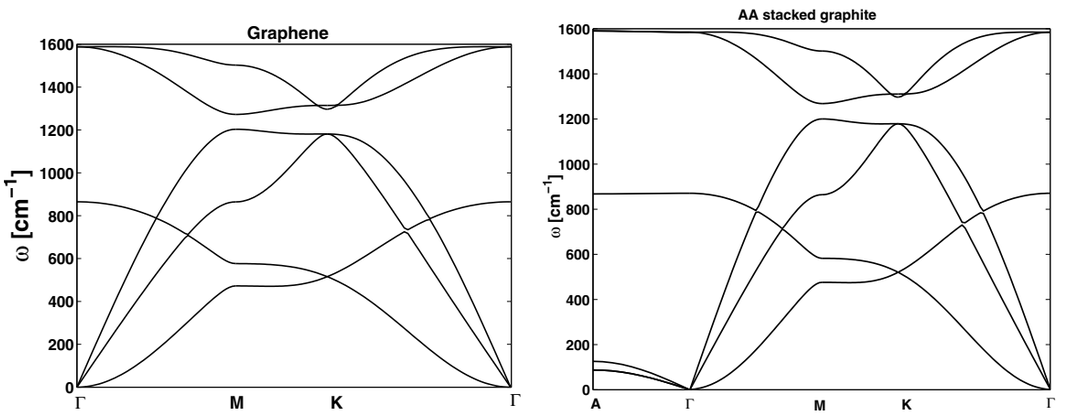

(a) Graphene (b) AA-stacked 3D graphite

Fig. 5. The calculated phonon dispersions of graphene (a), and AA-stacked 3D graphite (b).

The phonon dispersions for AA- and AB-stacked MLGS with an arbitrary layer number N can be calculated. In Fig. 7, the frequency of the intra-layer optical C-C stretching mode (Fig. 6(a))

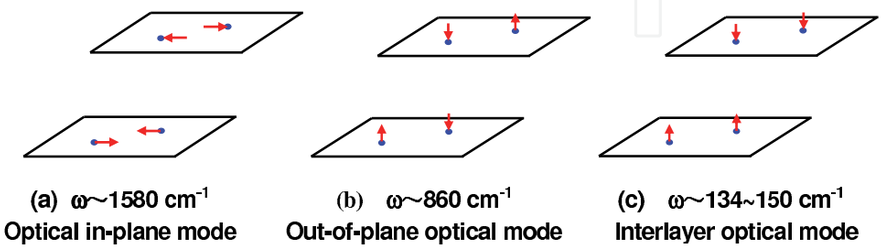

Fig. 6. Modality of atomic movements for three kinds of optical phonon modes in multilayered graphene systems.

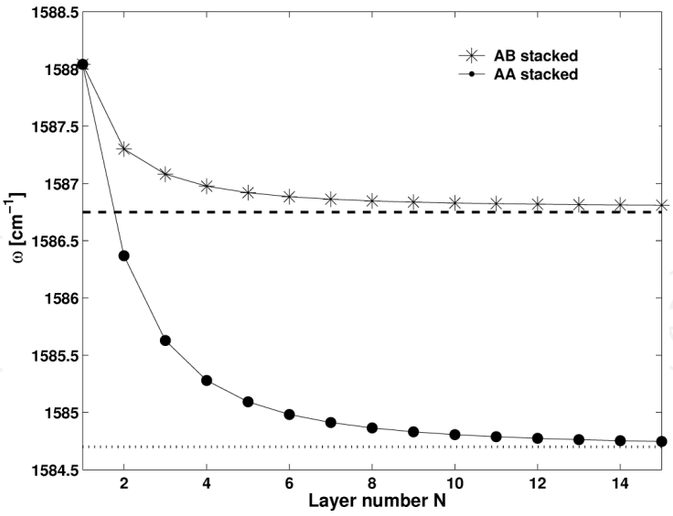

Fig. 7. The calculated frequency value for the optical C-C stretching mode vs the layer number N. Lines are draw to guide eyes.

in long wave length limit is represented as layer number N for AA- and AB-stacked MLGS. The layer number dependence of the frequency behaves a red shift as number increase which is in agreement with the experimental measurements. The frequency for this mode is about 1588 cm^{-1} in the single graphene layer, decreases with N increase, and almost saturates at about $N = 10$. The 3D limit is 1586.7 cm^{-1} (1584.7 cm^{-1}) for the AB- (AA-) stacked system. The amount of red shift value in the theoretical calculation corresponds excellently with that measured by experiments within the ranges $3 \sim 5$, $5 \sim 6$, and 8 cm^{-1} in Refs (Ferrari et al., 2006), (Gupta et al., 2006), and (Das et al., 2008), respectively.

At Γ point, the out-of-plane optical mode (Fig. 6(b)) is Ir active in the AB-stacked MLGS for both even and odd layer number (belong to A_{2u} irreducible representation). It is neither Raman active nor Ir active in the AA-stacked MLGS irrespective of the even-oddness of the layer number N. The optical activeness of the mode is useful in determining whether the MLGS is of AB- or AA-stacking. The frequency of the mode as the function of layer number N is shown in Fig. 8. In contrast to the C-C stretching optical mode, the frequency of the out-of-plane mode raises from 864.8 cm^{-1} to 872.6 cm^{-1} and exhibits a blue shift as layer number increase which could be identified with the development of the experimental technique.

For the inter-layer optical mode, the layer number dependence of long wave length frequency is shown in Fig. 9. This mode takes the greatest advantage of the inter-layer interaction and is considerably dependent on the layer number N as well as the stack style. When $N = 2$, this mode has the frequencies 106 cm^{-1} and 94.5 cm^{-1} for the AB- and AA-stacked MLGS respectively. The frequencies increase with increasing N and almost saturate at about $N = 10$. The 3D limit values are 149.8 cm^{-1} and 133.6 cm^{-1} for the AB- and AA-stacked MLGS respectively. The frequency differences as well as the alternation of Raman and Ir active of the mode might inspire considerably experimental interesting. For comparison, we plot the low-frequency phonon dispersions of the AB-stacked 2-layer system and 3D AB-stacked graphite in the same Fig. 10. The frequencies of the low-frequency optical modes in the 2-layer graphene are much smaller than their counterparts in the 3D graphite. For three acoustic modes shown in Fig. 10, because there is no $\hat{C}_4$ symmetry in the systems, two linear acoustic

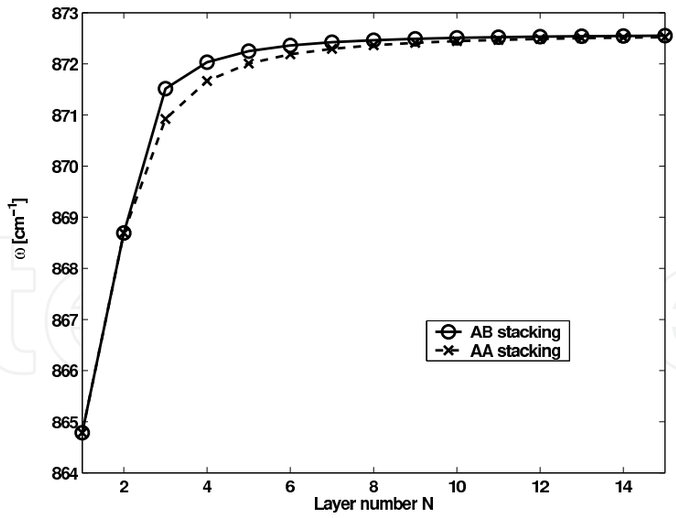

Fig. 8. The calculated frequency value for the out-of-plane optical mode vs the layer number N. This mode is Ir active in the AB stacking while it is neither Ir nor Raman active in the AA stacking. Lines are draw to guide eyes.

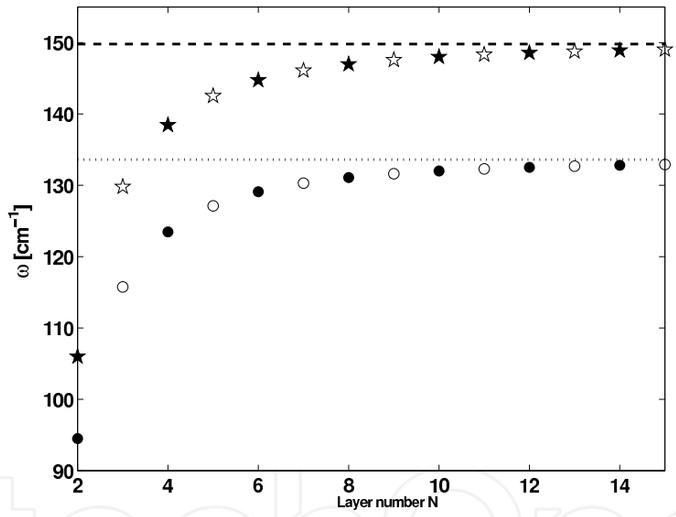

Fig. 9. The frequencies of the inter-layer optical mode vs the layer number N. Datas for the AB- and AA-stacked MLGS are designated by pentagrams and circles, respectively. The Raman and Infra-red activities for this mode are displayed by the full and empty symbols, respectively. The broken and dashed lines correspond to the frequencies of corresponding 3D graphite, respectively.

modes have different dispersions. And the third one marked in Fig. 10 is the flexure modes with quadratic dispersions near Γ point.

4. The effect of three-fold rotation symmetry of graphene on nanotubes

As constrain imposed by three-fold rotation symmetry $\hat{C}_3$, all the physical quantities of graphene have the same symmetry property. Consequently, the physical quantities of a single wall carbon nanotube (SWCNT), which can be viewed as wrapped graphene stripes,

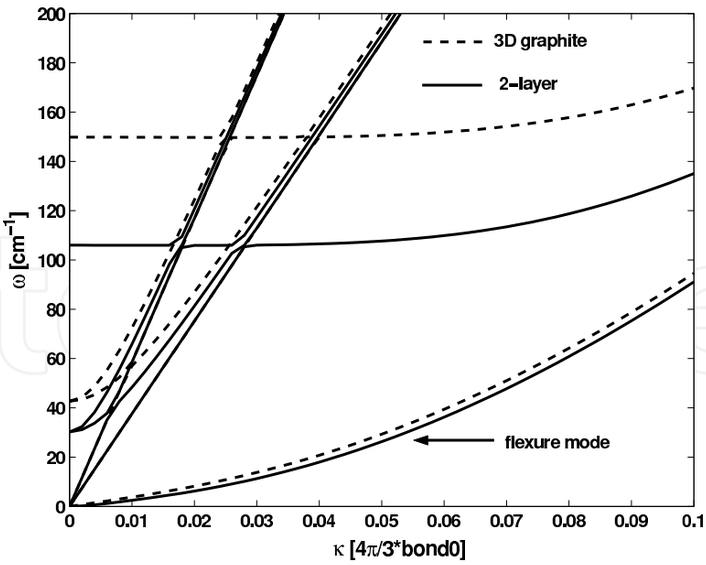

Fig. 10. In the low frequency region, there is significant difference between 3D AB-stacked graphite and the 2-layer AB-stacked graphene.

should also reserve some kind of similar symmetry property. It will manifest itself as the three-theta dependence for all physical quantities. In this section we will analysis this universal three-theta role in detail.

We start with the definition of a chiral vector for SWCNT as $\vec{R} = n_1\vec{a}_1 + n_2\vec{a}_2$ on the graphene lattice planer sheet, where $\vec{a}_1$ and $\vec{a}_2$ are the primitive lattice vectors (see Fig. 1) and (n_1, n_2) a pair of integers (Saito et al., 1998). Equivalently, a nanotube can also be denoted by the radius r and chiral angle θ (z axis is set parallel to the tube axis). They have the relations as

$$r = \frac{|\vec{a}_1|}{2\pi}\sqrt{n_1^2 + n_1 n_2 + n_2^2}, \qquad \theta = \arctan\frac{\sqrt{3}n_2}{2n_1 + n_2} \ . \tag{9}$$

We may establish a mapping from the space of chiral vectors on the planar sheet to that of the nanotube structure in a fixed way of wrapping

$$f : \{\text{chiral vector set}\} \mapsto \{\text{nanotube set}\} \ .$$

However this is not a one-to-one mapping. As mentioned in Ref. (Ye et al., 2006), a given SWCNT can be equivalently composed by three chiral vectors $\vec{R}_0$, $\vec{R}_2$ and $\vec{R}_4$ with chiral angles as θ, $\theta + 2\pi/3$ and $\theta + 4\pi/3$ respectively within the corresponding graphene sheet. Due to the $\hat{C}_6 = \hat{C}_3\hat{C}_2$ symmetry of the hexagonal graphene lattice sheet, there is another set of vectors $\vec{R}_1$, $\vec{R}_3$ and $\vec{R}_5$ with chiral angles as $\theta + \pi/3$, $\theta + \pi$ and $\theta + 5\pi/3$ respectively on the graphene sheet. These three chiral vectors correspond again to the same SWCNT which is actually the nanotube by rotating the tube formed by $\vec{R}_0$ upside down, i.e. a $\hat{C}_{2x}$ operation. The net result of the operation is an exchange of A and B carbon atoms in unit cells with the sign of its chiral index $\nu = \text{mod}\{n_1 - n_2, 3\}$ also changed. There is one another operation $\hat{\sigma}_{xz}$ connecting a pair of SWCNT which is the mirror reflection onto each other with respect to xz plane. Correspondingly $\vec{R}_0$ in the sheet is changed into its countpart $\vec{R}_0'$ with $\theta \to -\theta$ but ν

kept unchanged. These vectors, as shown in Fig. 11, have the explicit forms

$$\begin{aligned}
\vec{R}_0 &= n_1\vec{a}_1 + n_2\vec{a}_2, \\
\vec{R}_2 &= -(n_1+n_2)\vec{a}_1 + n_1\vec{a}_2, \\
\vec{R}_4 &= n_2\vec{a}_1 - (n_1+n_2)\vec{a}_2, \\
\vec{R}_1 &= -n_2\vec{a}_1 + (n_1+n_2)\vec{a}_2, \\
\vec{R}_3 &= -n_1\vec{a}_1 - n_2\vec{a}_2, \\
\vec{R}_5 &= (n_1+n_{2)}\vec{a}_1 - n_1\vec{a}_2, \\
\vec{R}_0' &= (n_1+n_2)\vec{a}_1 - n_2\vec{a}_2 \ .
\end{aligned} \tag{10}$$

Obviously, all these seven chiral vectors have the same radius.

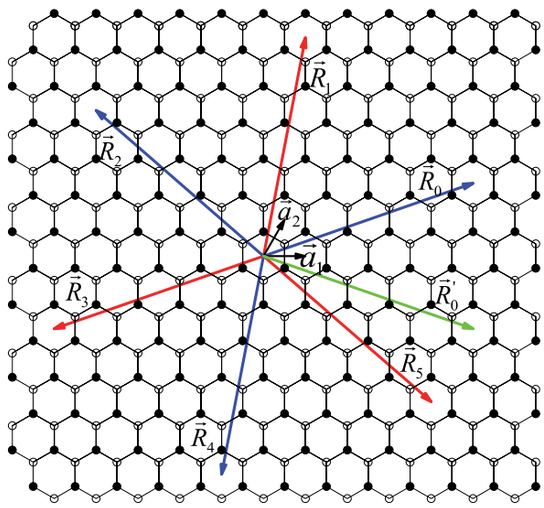

Fig. 11. Illustration of hexagonal lattice. A set of chiral vectors are shown after the symmetric operations on $\vec{R}_0$.

As one of the direct consequences of the above observations, any physical quantity $Q^\nu(r,\theta)$ of the SWCNT should be a periodical function of the chiral angle θ with period $\frac{2\pi}{3}$, i.e., $Q^\nu(r,\theta)$ can be expanded as (Ye et al., 2006)

$$Q^\nu(r,\theta) = \sum_{n=0}^{\infty} a_n^\nu \cos(3n\theta) + b_n^\nu \sin(3n\theta) \ . \tag{11}$$

This is an universal triple chiral angle (3θ) dependence of the SWCNT, which is actually the heritage of the three-fold rotational symmetry of graphene.
The permutation symmetry of the two carbon atoms in one unit cell would further give out the symmetry constrain under the operation $\theta \to \theta + \pi/3$. That is any scalars S keep unchanged, so do the radial components of the normal vectors, the azimuthal and axial components of the normal vectors change signs under the $\pi/3$ rotation in graphene plane (Jiang et al., 2008, a):

$$\begin{cases} S^\nu(\theta+\frac{\pi}{3}) = S^{-\nu}(\theta) \ , \\ \vec{v}^\nu(\theta+\frac{\pi}{3}) = \hat{C}_{2x}\vec{v}^{-\nu}(\theta) \end{cases} \tag{12}$$

with $\hat{C}_{2x}\vec{e}_r = \vec{e}_r$, $\hat{C}_{2x}\vec{e}_\phi = -\vec{e}_\phi$, $\hat{C}_{2x}\vec{e}_z = -\vec{e}_z$. Here $\vec{e}_r$, $\vec{e}_\phi$ and $\vec{e}_z$ are unit vectors oriented towards radial, azimuthal and axial directions upon the cylindrical surface respectively.
In addition, the symmetry operation $\hat{\sigma}_{xz}$ emerged in SWCNT gives that any scalars or radial and axial components of vectors are even functions of θ, while azimuthal components are odd,

$$\begin{cases} S^\nu(-\theta) = S^\nu(\theta) \ , \\ \vec{v}^\nu(-\theta) = \hat{\sigma}_{xz}\vec{v}^\nu(\theta) \end{cases} \tag{13}$$

with $\hat{\sigma}_{xz}\vec{e}_r = \vec{e}_r$, $\hat{\sigma}_{xz}\vec{e}_\phi = -\vec{e}_\phi$, $\hat{\sigma}_{xz}\vec{e}_z = \vec{e}_z$. Combined these symmetry restrictions Eqs (12) and (13), the general expression Eq. (11) can be further reduced. Taking the physical quantities of lattice dynamics as examples, we write the final expansions with all above symmetry restrictions considered in the following (Jiang et al., 2008, a).
The frequency ω of phonon is a scalar,

$$\begin{aligned} &\omega^\pm(\theta) = a_0 \pm a_1\cos(3\theta) + a_2\cos(6\theta) \pm a_3\cos(9\theta) + \ldots ; \\ &\omega^0(\theta) = a_0 + a_2\cos(6\theta) + \ldots \ . \end{aligned} \tag{14}$$

The three components of a vector can be expanded as

$$\begin{aligned} v_r^\nu(\theta) &= \sum_{n=0}^{\infty} \nu^{\lfloor\frac{1-(-1)^n}{2}\rfloor} a_n \cos 3n\theta = a_0 + \nu a_1\cos 3\theta + a_2\cos 6\theta + \ldots \ , \\ v_\phi^\nu(\theta) &= \sum_{n=0}^{\infty} \nu^{\lfloor\frac{1+(-1)^n}{2}\rfloor} b_n \sin 3n\theta = b_1\sin 3\theta + \nu b_2\sin 6\theta + \ldots \ , \\ v_z^\nu(\theta) &= \sum_{n=0}^{\infty} \nu^{\lfloor\frac{1+(-1)^n}{2}\rfloor} a_n \cos 3n\theta = \nu a_0 + a_1\cos 3\theta + \nu a_2\cos 6\theta + \ldots \ . \end{aligned} \tag{15}$$

Different from those physical quantities of normal vectors, the phonon polarization vector can be measured up to a global phase factor as ± 1. Therefore, the corresponding transformation properties with respect to the operations $\theta \to \theta + \frac{\pi}{3}$ and $\theta \to -\theta$ need to be generalized to

$$\begin{cases} v_P^{\nu(m)}(\theta + \frac{\pi}{3}) = \lambda^{(m)}(\hat{C}_{2x})\hat{C}_{2x}v_P^{-\nu(m)}(\theta) \ , \\ v_P^{\nu(m)}(-\theta) = \lambda^{(m)}(\hat{\sigma}_{xz})\hat{\sigma}_{xz}v_P^{\nu(m)}(\theta) \ , \end{cases} \tag{16}$$

respectively, where $\lambda^{(m)}(\hat{o})$ is a phase factor taking value either 1 or -1 depending on which phonon mode m we considered among $\vec{e}_r$ acoustic (AC), $\vec{e}_\phi$ optical (OP) and $\vec{e}_z$ OP modes (these three modes are non-zero frequency modes of SWCNT in long wave length limit which will be discussed in the next section) and on what kind of the symmetry operations $\hat{o}$ is applied, such as $\hat{C}_{2x}$ and $\hat{\sigma}_{xz}$. In particular,

$$\begin{aligned} \lambda^{(\vec{e}_r\mathrm{AC})}(\hat{C}_{2x}) &= \ \ \lambda^{(\vec{e}_r\mathrm{AC})}(\hat{\sigma}_{xz}) = \ \ 1 \ , \\ \lambda^{(\vec{e}_\phi\mathrm{OP})}(\hat{C}_{2x}) &= \ \ \lambda^{(\vec{e}_\phi\mathrm{OP})}(\hat{\sigma}_{xz}) = -1 \ , \\ \lambda^{(\vec{e}_z\mathrm{OP})}(\hat{C}_{2x}) &= -\lambda^{(\vec{e}_z\mathrm{OP})}(\hat{\sigma}_{xz}) = -1 \ . \end{aligned} \tag{17}$$

The detailed expressions of polarization vectors with $\lambda^m(\sigma_{xz}) = -1$, and $\lambda^m(C_{2x}) = -1$ are

$$\begin{aligned}
v_r^\nu(\theta) &= \sum_{n=0}^{\infty} \nu^{[\frac{1+(-1)^n}{2}]} b_n \sin 3n\theta = b_1 \sin 3\theta + \nu b_2 \sin 6\theta + \dots , \\
v_\phi^\nu(\theta) &= \sum_{n=0}^{\infty} \nu^{[\frac{1-(-1)^n}{2}]} a_n \cos 3n\theta = a_0 + \nu a_1 \cos 3\theta + a_2 \cos 6\theta + \dots , \\
v_z^\nu(\theta) &= \sum_{n=0}^{\infty} \nu^{[\frac{1-(-1)^n}{2}]} b_n \sin 3n\theta = \nu b_1 \sin 3\theta + b_2 \sin 6\theta + \dots .
\end{aligned} \tag{18}$$

While for $\lambda^m(\sigma_{xz}) = 1$, and $\lambda^m(C_{2x}) = -1$, the polarization vectors can be expressed as

$$\begin{aligned}
v_r^\nu(\theta) &= \sum_{n=0}^{\infty} \nu^{[\frac{1+(-1)^n}{2}]} a_n \cos 3n\theta = \nu a_0 + a_1 \cos 3\theta + \nu a_2 \cos 6\theta + \dots , \\
v_\phi^\nu(\theta) &= \sum_{n=0}^{\infty} \nu^{[\frac{1-(-1)^n}{2}]} b_n \sin 3n\theta = \nu b_1 \sin 3\theta + b_2 \sin 6\theta + \dots , \\
v_z^\nu(\theta) &= \sum_{n=0}^{\infty} \nu^{[\frac{1-(-1)^n}{2}]} a_n \cos 3n\theta = a_0 + \nu a_1 \cos 3\theta + a_2 \cos 6\theta + \dots .
\end{aligned} \tag{19}$$

Then for $\lambda^m(\sigma_{xz}) = -1$, and $\lambda^m(C_{2x}) = 1$, they are

$$\begin{aligned}
v_r^\nu(\theta) &= \sum_{n=0}^{\infty} \nu^{[\frac{1-(-1)^n}{2}]} b_n \sin 3n\theta = \nu b_1 \sin 3\theta + b_2 \sin 6\theta + \dots , \\
v_\phi^\nu(\theta) &= \sum_{n=0}^{\infty} \nu^{[\frac{1+(-1)^n}{2}]} a_n \cos 3n\theta = \nu a_0 + a_1 \cos 3\theta + \nu a_2 \cos 6\theta + \dots , \\
v_z^\nu(\theta) &= \sum_{n=0}^{\infty} \nu^{[\frac{1+(-1)^n}{2}]} b_n \sin 3n\theta = b_1 \sin 3\theta + \nu b_2 \sin 6\theta + \dots .
\end{aligned} \tag{20}$$

For the second rank tensor ϵ, the helical symmetry of SWCNT results (Damnjanović et al., 1999)

$$\begin{aligned}
&\epsilon_{xx} = \epsilon_{yy}, \\
&\epsilon_{xx} = -\epsilon_{yy}, \\
&\epsilon_{xz} = \epsilon_{yz} = \epsilon_{zx} = \epsilon_{zy} = 0.
\end{aligned} \tag{21}$$

Similar to the analysis above, it is obtained (Ye et al., 2006) that

$$\begin{aligned}
&\epsilon_{ii}^{(\nu)}(\theta + \pi/3) = \epsilon_{ii}^{(-\nu)}(\theta), \\
&\epsilon_{ii}^{(\nu)}(-\theta) = \epsilon_{ii}^{(\nu)}(\theta), \\
&\epsilon_{xy}^{(\nu)}(\theta + \pi/3) = -\epsilon_{xy}^{(-\nu)}(\theta), \\
&\epsilon_{xy}^{(\nu)}(\theta + \pi/3) = \epsilon_{xy}^{(-\nu)}(\theta), \\
&\epsilon_{xy}^{(\nu)}(-\theta) = -\epsilon_{xy}^{(\nu)}(\theta),
\end{aligned} \tag{22}$$

where $i = x, y, z$. By noticing that the diagonal term is unchanged when the tube is reversed or reflected, and off-diagonal term vanishes, then

$$\begin{aligned}
\epsilon_{ii}^{(\pm)} &= a_0 \pm a_1 \cos(3\theta) + a_2 \cos(6\theta) + \cdots , \\
\epsilon_{ii}^{(0)} &= a_0 + a_2 \cos(6\theta) + a_4 \cos(12\theta) + \cdots , \\
\epsilon_{xy}^{(\nu)} &= 0 .
\end{aligned} \tag{23}$$

The coefficients $a_n's$ for different chirality have no direct relationships.

5. Coordinate systems in carbon nanotubes

As stated in the above section, an SWCNT can be identified by a chiral vector $\vec{R} = n_1\vec{a}_1 + n_2\vec{a}_2$ defined on the graphene lattice sheet with (n_1, n_2) a pair of integers. A graphene stripe is obtained by cutting the graphene sheet along the direction perpendicular to $\vec{R}$, which ensures the same edge structures of the two sides of the stripe. A nanotube is formed by wrapping the stripe, or vice verse, the stripe is the unfold plane of the nanotube. Obviously, $\vec{R}$ corresponds to the circumference of the tube and $\frac{\vec{R}}{N}$ $(N = \mathrm{GCD}(n_1, n_2))$ corresponds to a pure rotational symmetry operation $\hat{C}_N$ of the tube. Along the tube axis, i.e. z axis, a translational vector $\vec{T}$ can be defined as $\vec{T} \cdot \vec{R} = 0$ and its corresponding translation symmetry operation is $\hat{T}$. In the frame of $(\vec{a}_1, \vec{a}_2)$, it is $\vec{T} = t_1\vec{a}_1 + t_2\vec{a}_2$ with

$$t_1 = -\frac{2n_2 + n_1}{M}, \quad t_2 = \frac{2n_1 + n_2}{M}, \quad (M = \mathrm{GCD}(2n_2 + n_1, 2n_1 + n_2)).$$

It can be further obtained that

$$|\frac{\vec{R}}{N} \times \vec{T}| = \frac{n_1(2n_1 + n_2) + n_2(2n_2 + n_1)}{NM} |\vec{a}_1 \times \vec{a}_2| \equiv N_T |\vec{a}_1 \times \vec{a}_2|.$$

Because $N_T \geq 1$, the set $(\frac{\vec{R}}{N}, \vec{T})$ cannot be used as the primitive lattice vectors in unfold plane. The one-dimensional (1D) single wall carbon nanotubes belong to 1D line groups (Damnjanović et al., 1999; 2000). For chiral nanotubes, the definition of the primary chiral operation is not unique. Correspondingly, the different choices of primitive translational vectors exist on the unfold plane. Any proper pair of vectors which can map all lattice points on stripe can form the unit cell. In SWCNT, these two vectors correspond to two primitive chiral operations. There are two commonly used coordinates (Saito et al., 1998; White et al., 1993). The first one uses the rotational $\hat{C}_N$ and helical $\hat{S}_1(\alpha, h)$ symmetry descriptions for SWCNT(White et al., 1993), i.e. $\frac{\vec{R}}{N}$ and $\vec{H}$ as the primitive lattice vectors on unfold plane, which will be called White coordinate hereafter. Another chooses translational $\hat{T}$ and helical $\hat{S}_2(\alpha_0, h_b)$ symmetry descriptions with $\vec{T}$ and $\vec{Q}$ on unfold plane referred as Dresselhaus coordinate (Saito et al., 1998). The unit cells on unfold plane for two coordinate systems are shown in Fig. 12(a). Under the definition of $|\frac{\vec{R}}{N} \times \vec{H}| = |\vec{a}_1 \times \vec{a}_2|$ or $|\vec{T} \times \vec{Q}| = |\vec{a}_1 \times \vec{a}_2|$, some

useful relations can be obtained (the arbitrariness of sign has be fixed),

$$\begin{cases} R = \sqrt{n_1^2 + n_2^2 + n_1 n_2}\ |\vec{a}_1|, \\ T = \frac{\sqrt{3}}{M}\sqrt{n_1^2 + n_2^2 + n_1 n_2}\ |\vec{a}_1|\ , \end{cases} \tag{24}$$

$$\begin{cases} \vec{H} = p_1\vec{a}_1 + p_2\vec{a}_2, \\ n_1 p_2 - n_2 p_1 = N\ , \end{cases} \tag{25}$$

$$\begin{cases} \vec{Q} = q_1\vec{a}_1 + q_2\vec{a}_2, \\ q_1(2n_1 + n_2) + q_2(2n_2 + n_1) = M\ . \end{cases} \tag{26}$$

The rotation angles α (α_0) as well as translations along z axis h (h_b) in helical symmetry operations can be derived by projecting $\vec{H}$ ($\vec{Q}$) to the directions of $\vec{R}$ and $\vec{T}$ respectively,

$$\begin{aligned} \vec{H}\cdot\frac{\vec{R}}{R} \equiv \frac{R}{2\pi}\alpha \Rightarrow \alpha &= 2\pi\frac{(2n_1+n_2)p_1 + (2n_2+n_1)p_2}{(2n_1+n_2)n_1 + (2n_2+n_1)n_2}, \\ \vec{H}\cdot\frac{\vec{T}}{T} \equiv h \Rightarrow h &= \frac{\sqrt{3}N}{2\sqrt{n_1^2+n_2^2+n_1n_2}}|\vec{a}_1|\ , \end{aligned} \tag{27}$$

$$\begin{aligned} \vec{Q}\cdot\frac{\vec{R}}{R} \equiv \frac{R}{2\pi}\alpha_0 \Rightarrow \alpha_0 &= 2\pi\frac{M}{(2n_1+n_2)n_1 + (2n_2+n_1)n_2}, \\ \vec{H}\cdot\frac{\vec{T}}{T} \equiv h_b \Rightarrow h_b &= \frac{\sqrt{3}(n_1q_2 - n_2q_1)}{2\sqrt{n_1^2+n_2^2+n_1n_2}}|\vec{a}_1|\ . \end{aligned} \tag{28}$$

Before go to the reciprocal space and discuss the good quantum numbers within two coordinate systems, we introduce four important integers and review their geometric meanings.

$$N_T = \frac{T}{h} = \frac{n_1(2n_1+n_2) + n_2(2n_2+n_1)}{MN}\ , \tag{29}$$

$$N_D = N_T N = \frac{2\pi}{\alpha_0} = \frac{n_1(2n_1+n_2) + n_2(2n_2+n_1)}{M}\ , \tag{30}$$

$$N_b = \frac{h_b}{h} = \frac{n_1q_2 - n_2q_1}{N}\ , \tag{31}$$

$$\Omega = \frac{\alpha}{\alpha_0} = N_D\frac{\alpha}{2\pi} = \frac{(2n_1+n_2)p_1 + (2n_2+n_1)p_2}{M}\ . \tag{32}$$

From above formulae, it shows that N_T is the number of White unit cells stacked along the tube axis to form a minimum translation period; N_D represents, in one side, the unit cell numbers in tubular section with height T called as a “giant" cell, or in the other side, the times of minimum rotation angle α_0 in one circle; N_b describes the ratio of translations along tube

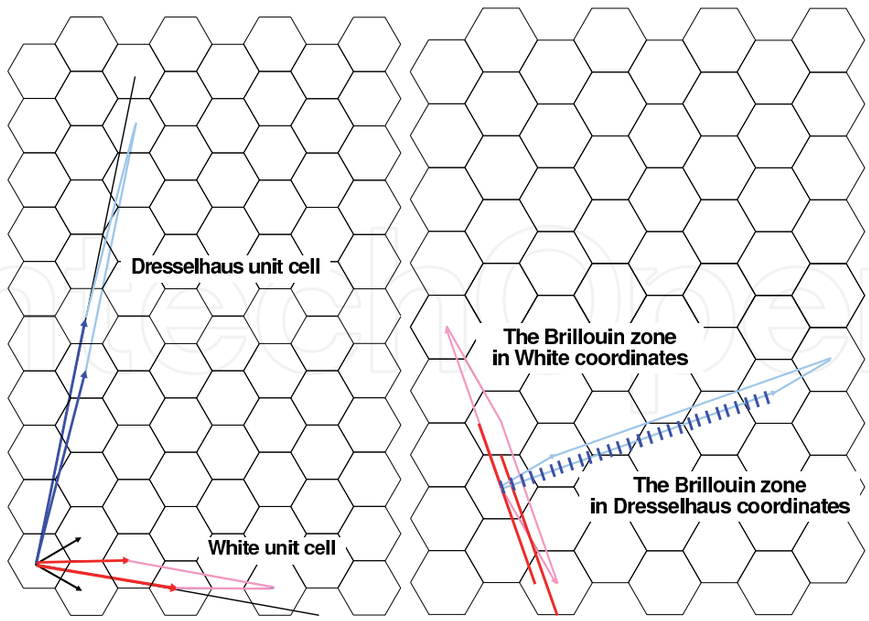

(a) Unfold plane of nanotube (b) Reciprocal lattice on unfold plane

Fig. 12. The unfold plane (a) and reciprocal lattice (b) of the nanotube $(4,\ 2)$. The unit cells and primitive lattice vectors of White $\{\vec{R}/N,\ \vec{H}\} \leftrightarrow \{\hat{C}_N,\ \hat{S}_1(\alpha,h)\}$ and Dresselhaus $\{\vec{T},\ \vec{Q}\} \leftrightarrow \{\hat{T},\ \hat{S}_2(\alpha_0,h_b)\}$ coordinates are shown in (a). The Brillouin zones and quantum numbers of White $\{n,\ \kappa\}$ and Dresselhaus $\{k_z,\ n_i\}$ are shown in (b).

axis of the two helical symmetry operations; and Ω is the ratio of rotation angles of the two helical operations, which can be proved to be relatively prime with N_T.
The 1D group characters of symmetry operators in White and Dresselhaus coordinates can be written respectively as:

$$\begin{aligned} \{\hat{C}_N,\ \hat{S}_1(\alpha,h)\} &\longrightarrow \{e^{i\frac{2\pi}{N}n},\ e^{i\kappa}\} \quad \text{for White coordinate,} \\ \{\hat{T},\ \hat{S}_2(\alpha_0,h_b)\} &\longrightarrow \{e^{iN_Tk_zT},\ e^{i\kappa'}\} \quad \text{for Dresselhaus coordinate.} \end{aligned} \tag{33}$$

The prefix N_T on the character $e^{iN_Tk_zT}$ is for taking the same length units for two coordinate systems. Using the periodical boundary conditions and notice that $\hat{S}_2^{N_D}(\alpha_0,h_b) = \hat{S}_2(2\pi,N_bNT) = \hat{T}^{N_bN} \to e^{iN_D\kappa'} = e^{iN_bNN_Tk_zT}$, it is

$$n = 0,1,\ldots,N-1\ , \tag{34}$$

$$\kappa \in [\ 0,2\pi)\ , \tag{35}$$

$$k_z \in [\ 0,2\pi/N_TT)\ , \tag{36}$$

$$\kappa' = N_bk_zT + \frac{2\pi}{N_D}n_i\ , \tag{37}$$

$$n_i = 0,1,\ldots,N_D-1\ . \tag{38}$$

According to symmetry operators, the good quantum numbers in the two coordinate system should be $\{n,\kappa\}$ and $\{k_z,\kappa'\}$ respectively. But as seen from Eq. (38), κ' has a complicate form,

it is commonly to use $\{k_z, n_i\}$ instead of $\{k_z, \kappa'\}$ as "good quantum number" in Dresselhaus coordinate. Since the nanotube has no $\hat{C}_{N_D}$ symmetry, which is only an isogonal group of the symmetry group of the nanotube, strictly speaking, n_i is not a good angular quantum number of the rotational symmetry as seemed to be.
For deducing the relations between two sets of quantum numbers, the following equivalence is used:

$$\begin{aligned} \hat{C}_N &= \hat{S}_2^{N_T}(\alpha_0, h_b)\hat{T}^{-N_b}, \\ \hat{T} &= \hat{S}_1^{N_T}(\alpha, h)\hat{C}_N^{-\Omega}, \\ \hat{S}_1(\alpha, h) &= \hat{S}_2^{\Omega}(\alpha_0, h_b)(\hat{T}^{1/N_T})^{-(\Omega N_b - 1)}. \end{aligned} \tag{39}$$

Then from the characters of the operations, it is followed that

$$\begin{aligned} \frac{2\pi}{N} n &= \frac{2\pi}{N} n_i + 2\pi \mathcal{I}_1, \\ N_T k_z T &= N_T \kappa - N_T n\alpha + 2\pi \mathcal{I}_2, \\ \kappa &= n_i \alpha + k_z T + 2\pi \mathcal{I}_3, \end{aligned} \tag{40}$$

where $\mathcal{I}_1$, $\mathcal{I}_2$, and $\mathcal{I}_3$ are arbitrary integers. The first two of Eq. (40) give the following relations directly,

$$n = n_i \pmod N, \quad \text{or} \quad n_i = n + NJ \quad (J \text{ an integer}), \tag{41}$$

$$k_z = \frac{2\pi}{N_T T} \text{Frac}\left(N_T \frac{\kappa - n\alpha}{2\pi} \right). \tag{42}$$

The third of Eq. (40) contains fraction and integer parts of information. From its fraction part,

$$\kappa = 2\pi \text{Frac}\left(\frac{k_z T + n_i \alpha}{2\pi} \right). \tag{43}$$

From the integer part,

$$J\,\Omega = \text{Int}\left[N_T \frac{\kappa - n\alpha}{2\pi} - \text{Frac}\left(N_T \frac{\kappa - n\alpha}{2\pi} \right) \right] \pmod{N_T}. \tag{44}$$

The equations (41), (42), (43), and (44) provide the complete relations between the two sets of quantum numbers (Tang et al., 2009). The Brillouin zones and quantum numbers $\{n,\ \kappa\}$ and $\{k_z,\ n_i\}$ are shown in Fig. 12(b). Actually, Eq. (44) can uniquely determine the integer J and shows the nontrivial relation between n and n_i. Interested readers can refer monographs about number theory.

6. Lattice dynamics of single-wall carbon nanotubes

6.1 Vibrational potentials

We discuss the lattice dynamics of single-wall carbon nanotubes (SWCNT) within the White coordinate system (White et al., 1993) which has been described detailed in the above section. Setting the z axis along the tube axis and the x axis across the middle point of a C-C bond, any unit cell in the (n_1, n_2) or equivalently $(r,\ \theta)$ tubule can be notated by a pair of integers (m, l):

$$\vec{r}_{m,l} = m\vec{H} + l\frac{\vec{R}}{N}. \tag{45}$$

In other words, any unit cell on SWCNT can be covered by m screw operations $\hat{S}_1(\alpha, h)$ and l rotations $\hat{C}_N$ successively (see the details in section 4).

Again, we use the idea of five distinctive terms (Aizawa et al., 1990) for the potential of graphene sheet, and extend them to the nanotube cases. What we stress is that the satisfying of the rigid translational and rotational invariance must be kept in the generalization, i.e., the potential energy must keep unchanged term by term when the tube is rigidly translated or rotated around any axis. Introduce $\vec{r}_i$ as the equilibrium position of atom i and $\vec{u}_i$ as its displacement vector. $\vec{r}_{ij} = \vec{r}_j - \vec{r}_i$ is the vector from atom i to j in the nanotube while the modulus r_{ij} represents the length of C-C bond between atoms i and j. The vector $\vec{r}_i$ is determined following the geometry of a warped graphene sheet. Unlike that in graphene, the geometrical curvature results to that not only the three tridental bond lengths nearest-neighbored with the atom i but also the angles between any of the two bonds are not equal to each other even in equilibrium position, especially for thin tubes. We express in the following a detailed expression of the vibrational potential for the SWCNT with the curvature effect being carefully in-cooperated. It satisfies precisely the requirements of the rigid translational and rotational invariance and realizes the corresponding general symmetry sum rules in Ref. (Popov et al., 2000).

The five terms of potential energy are basically the same as those in graphene sheet with rigorous modification of unit vectors in the present case (Jiang et al., 2006). We list them in the following for completeness.

(1) V_l is the potential of the spring force between the nearest-neighbor atom pair,

$$V_l = \frac{k_l}{2} \sum_{i=2}^{4} [(\vec{u}_i - \vec{u}_1) \cdot \vec{e}^{\,l}_{1i}]^2 \,, \tag{46}$$

where k_l is the first-order force constant and $\vec{e}^{\,l}_{1i} = \frac{\vec{r}_{1i}}{|\vec{r}_{1i}|}$. We'd like to point out that the component of the displacement vectors perpendicular to $\vec{e}^{\,l}_{1i}$ violates the rigid rotational invariance and is forbidden.

(2) V_{sl} is also the potential of the spring force but between the next nearest-neighbored atoms illustrated as $(1, 5 \ldots 10)$ in Fig. 1,

$$V_{sl} = \frac{k_{sl}}{2} \sum_{i=5}^{10} [(\vec{u}_i - \vec{u}_1) \cdot \vec{e}^{\,l}_{1i}]^2 \tag{47}$$

with k_{sl} the second-order force constant.

(3) The potential energy for the in-surface bond bending V_{BB} with three atoms involved is more complicated than that in graphene planar sheet due to the curvature-resulted deviation of an equilibrium angle from a constant.

$$\begin{aligned} V_{BB} &= \frac{k_{BB}}{4} \sum_{j_i} \sum_{\substack{j'_i \\ (j'_i \neq j_i)}} \left[\frac{\vec{u}_{j_i} - \vec{u}_i}{r_{ij_i}} \cdot (\vec{e}^{\,l}_{ij'_i} - \cos\theta_{j_i i j'_i} \vec{e}^{\,l}_{ij_i}) + \frac{\vec{u}_{j'_i} - \vec{u}_i}{r_{ij'}} \cdot (\vec{e}^{\,l}_{ij_i} - \cos\theta_{j'_i i j_i} \vec{e}^{\,l}_{ij'_i}) \right]^2 \\ &= \frac{k_{BB}}{4} \sum_{j_i} \sum_{\substack{j'_i \\ (j'_i \neq j_i)}} (\cos\theta'_{j_i i j'_i} - \cos\theta_{j_i i j'_i})^2 \,. \end{aligned} \tag{48}$$

Where i, j_i, and j_i' take the same sites as those in graphene (see Eq. (3) and Fig. 1 in section 3). The difference is here $\theta_{j_i i j_i'}$ for the equilibrium angle between the bonds $\vec{r}_{ij_i}$ and $\vec{r}_{ij_i'}$ which is no more 120° in general. $\theta'_{j_i i j_i'}$ is for the corresponding angle in vibration. The bond angles are expressed in terms of $\vec{u}_{j_i} - \vec{u}_i$ and $\vec{u}_{j_i'} - \vec{u}_i$, which can be proved that the rigid rotational invariance referred to an arbitrary axis is kept only when the differences among bond lengths and bond angles be carefully accounted.
(4) Extending the out-of-surface bond bending V_{rc} term into SWCN,

$$V_{rc} = \frac{k_{rc}}{2}[(3\vec{u}_i - \sum_{j_i} \vec{u}_{j_i}) \cdot \vec{e}_i^{rc}]^2, \tag{49}$$

$$\vec{e}_i^{rc} = -\frac{\sum_{j_i} \vec{r}_{j_i}}{|\sum_{j_i} \vec{r}_{j_i}|}\ , \tag{50}$$

where i takes 1 or 2 with j_i running over the three nearest neighbors of atom i. Different from graphene, an unit vector $\vec{e}_i^{rc}$ is introduced for keeping the rigid rotational invariance. We show the difference between $\vec{e}_i^{rc}$ and radial unit vector $\vec{e}_1^{r}$ in Fig. 13. When the radius of tube is large enough, the vector $\vec{e}_i^{rc}$ is close enough to the $\vec{e}_1^{r}$. However, we stress that the potential term V_{rc} with $\vec{e}_i^{rc}$ substituted by $\vec{e}_i^{r}$ would break the rotational symmetry.

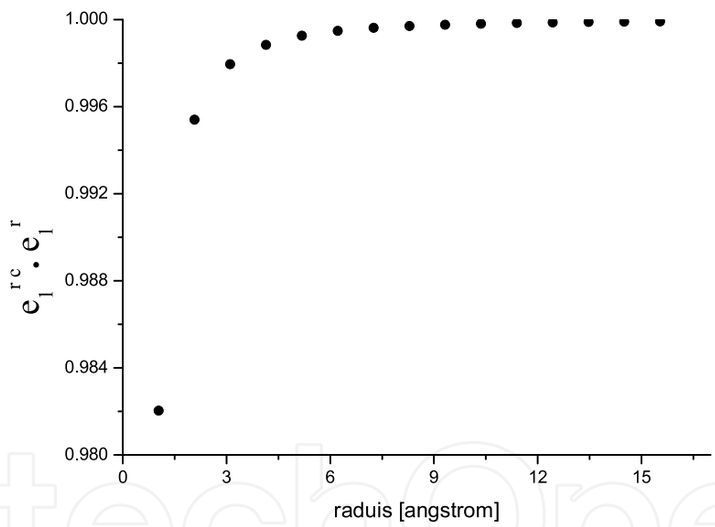

Fig. 13. The projection of $\vec{e}_1^{rc}$ on $\vec{e}_1^{r}$ for tubes $(2n, n)$ with $n \in [1, 15]$. It shows that $\vec{e}_1^{rc}$ only deviates about 2% from $\vec{e}_1^{r}$ even in the small radius (2, 1) tube.

(5) The twist potential energy for bond $\vec{r}_{1k}$ is generalized as

$$V_{tw} = \frac{k_{tw}}{2} \sum_{\langle i,j \rangle} [(\vec{u}_i - \vec{u}_j - (\vec{u}_{i'} - \vec{u}_{j'})) \cdot \vec{e}_{1k}^{r}]^2\ , \tag{51}$$

where $\vec{e}_{1k}^{r}$ is the unit vector along the radial direction of the middle point of $\vec{r}_{1k}$, $\langle i, j \rangle$ represents a pair of atoms nearest-neighbored with atom 1 while k the third of its nearest neighbors (see Fig. 1 for reference). Pair $\langle i', j' \rangle$ is the image of $\langle i, j \rangle$ referring to a $\hat{C}_2$ rotation around the axis in $\vec{e}_{1k}^{r}$.

Obviously, it can be checked that all above five potential energy terms satisfy the translational invariance (Jiang et al., 2006). When $\vec{u}_i = \vec{u}_j$, $\vec{u}_i - \vec{u}_j = 0$ leads to

$$V_l = V_{sl} = V_{BB} = V_{rc} = V_{tw} = 0 \ .$$

For the rotational invariance, we have to consider the five potentials term by term separately (Born & Huang, 1954; Madelung, 1978). When the tube rotates rigidly around an arbitrary axis for a small angle $\delta\vec{\omega}$ with its direction along the axis $\frac{\delta\vec{\omega}}{|\delta\vec{\omega}|}$, each lattice site acquires a displacement $\vec{u}_i = \delta\vec{\omega} \times \vec{r}_i$,

$$\vec{u}_i - \vec{u}_j = \delta\vec{\omega} \times (\vec{r}_i - \vec{r}_j) = \delta\vec{\omega} \times \vec{r}_{ji} \ . \tag{52}$$

Substituting Eq. (52) into the first two potential terms (46) and (47), it is straightforward to have $(\vec{u}_j - \vec{u}_i) \cdot \vec{e}^{\,l}_{ij} = r_{ij}(\delta\vec{\omega} \times \vec{e}^{\,l}_{ij}) \cdot \vec{e}^{\,l}_{ij} = 0$. Then

$$V_l = V_{sl} = 0 \ .$$

Substituting Eq. (52) into the third potential term (48), a typical representative term in summation becomes

$$V_{BB} \sim \frac{k_{BB}}{4}[\delta\vec{\omega} \cdot (\vec{e}^{\,l}_{12} \times \vec{e}^{\,l}_{13} + \vec{e}^{\,l}_{13} \times \vec{e}^{\,l}_{12})]^2 = 0 \ .$$

In which a fact has been used that r_{ij} in the denominate is canceled by that in the numerator when Eq. 52 is applied. Moreover, for each typical representative term in potentials (49) and (51), we have

$$V_{rc} \sim \tfrac{k_{rc}}{2}[\delta\vec{\omega} \times (\vec{r}_{12} + \vec{r}_{13} + \vec{r}_{14}) \cdot \vec{e}^{\,rc}_1]^2 = 0 \ ,$$
$$V_{tw} \sim \tfrac{k_{tw}}{2}[\delta\vec{\omega} \times (\vec{r}_{43} - \vec{r}_{56}) \cdot \vec{e}^{\,r}_{12}]^2 = 0 \ .$$

For further clarification, we show the phonon spectrum with all the bond lengths and bond angles assumed to be equal to that of the graphene in Fig. 14(a) for SWCNT (5,2). It shows clearly that the twisting mode (TW) at $(\kappa, n) = (0, 0)$ is no longer a zero mode and there is a finite gap with the order of 0.5 cm^{-1}. Although it is a minute number and entirely negligible in practice, it is of qualitative significance. When we take the proper bond lengths with about -1.3%, -0.3% and 0.0% shorter than that of graphene 1.42 Å respectively, the correct phonon spectrum is calculated and shown in Fig. 14(b) for the same SWCNT.

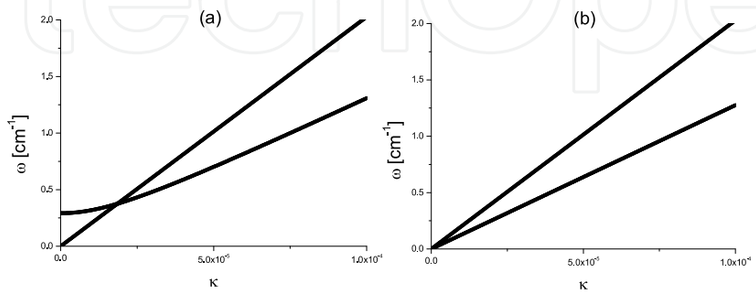

Fig. 14. The effect of bond lengths on TW mode in tube (5, 2). (a) All bonds are assumed to be the same. The frequency of TW mode at $\kappa = 0$ is nonzero. (b) The differences between bonds are considered. The frequency of TW mode is precisely zero.

As a one-dimensional system, SWCNT has a distinguished feature that the two degenerate transversal acoustic (TA) modes shown up at $(\kappa, n) = \pm(\alpha, 1)$ are flexure modes. Instead of the conventional linear behaviors, the low frequency limits of their dispersions are parabolic as $\omega^2 = \beta^2(\kappa \mp \alpha)^4$. We stress that the rigid rotational invariance around z axis itself is not a sufficient condition for the existence of the flexure modes. It can be declared more clearly by a counter example. By introducing a potential term $V_{\tau i} = \frac{k_{\tau i}}{2}[(\vec{u}_2 - \vec{u}_1) \cdot \vec{e}_{12}^{\tau i}]^2$ with $\vec{e}_{12}^{\tau i} = \vec{e}_{12}^{r} \times \vec{e}_{12}^{l}$, which satisfies $V_{\tau i} = 0$ when the tube rotates around the z axis, there will be no flexure mode in SWCNT (Dobardžić et al., 2003). This is because that $V_{\tau i}$ is not zero when the tube rotates around any axis perpendicular to the z axis.

By tuning the calculated results to the experimental data (Rao et al., 1997) for the Raman modes of (10, 10) tube (see Table 3), the corresponding force constants are fit as $k_l = 364.0\,\mathrm{Nm}^{-1}$, $k_{sl} = 62.0\,\mathrm{Nm}^{-1}$, $k_{BB} = 1.07 \times 10^{-11}$ erg, $k_{rc} = 14.8\,\mathrm{Nm}^{-1}$, and $k_{tw} = 6.24\,\mathrm{Nm}^{-1}$ (Jiang et al., 2006). For chiral SWCNT, all tubes belong to the fifth 1D line group (Popov et al., 2000) with two atoms in one unit cell and have six phonon modes at any point of reciprocal space . Looking at three specific points $(\kappa, n) = (0, 0)$, $(\kappa, n) = (\alpha, 1)$, and $(\kappa, n) = (2\alpha, 2)$, 18 phonon modes are successfully identified (Alon, 2001; Jiang et al., 2006). They are (I) 3 zero modes: two at $(\kappa, n) = (0, 0)$ as longitudinal acoustic (LA) and TW modes both belonging to ${}_0A_0^-$ representation (Reps), and one at $(\kappa, n) = (\alpha, 1)$ as the flexure mode; (II) 9 Raman active modes: three at $(\kappa, n) = (0, 0)$ belonging to ${}_0A_0^+$ Reps as $\vec{e}_r$ acoustic (AC), $\vec{e}_\theta$ optical (OP) and $\vec{e}_z$ OP, and six at $(\kappa, n) = (2\alpha, 2)$ belonging to the same ${}_{2\alpha}E_2$ Reps; (III) 1 Ir active mode: at $(\kappa, n) = (0, 0)$ as the OP mode with A and B atoms oscillating out of surface in tubular radial direction and belonging to ${}_0A_0^-$ Reps; (IV) 5 Raman and Ir active modes at $(\kappa, n) = (\alpha, 1)$ assigned to ${}_\alpha E_1$ Reps.

Reps	${}_0A_0^+$	${}_0A_0^+$	${}_\alpha E_1^-$	${}_\alpha E_1^-$	${}_{2\alpha}E_2^+$	${}_{2\alpha}E_2^+$	${}_{2\alpha}E_2^+$	${}_{2\alpha}E_2^+$
Theory	167	1588	105	1588	21	367	873	1584
Experiment (Rao et al., 1997)	186	1593	118	1567	/	377	/	1606

Table 3. Comparison between the calculated results and the experimental values for several mode frequencies (in the unit of cm^{-1}) of SWCNT (10,10).

6.2 Chiral angle and radius dependence of phonon properties

With the phenomenological vibration potential model described in above subsection, the phonon frequencies, acoustic velocities, and eigenvectors are calculated as the functions of radius and chiral angles, and further fitted following the three-fold symmetry expansion discussed in section 4. Because we are interested in SWCNT with smaller radius which should be quite different from those of graphene stripe, the fitting range is chosen as $r \in [4.0, 10.0]$ Å and $\theta \in [-\frac{\pi}{6}, \frac{\pi}{6}]$ for frequencies and velocities, $r \in [2.0, 10.0]$ Å and $\theta \in [-\frac{\pi}{3}, \frac{\pi}{3}]$ for polarization vectors. The relative errors in fitting are set less than 5×10^{-4}. The expansions of frequencies of Raman and Ir active modes, the velocities at $(\kappa, n) = (0, 0)$ and flexure parabolic at $(\kappa, n) = (\alpha, 1)$, and the polarization vectors of nonzero modes at $(\kappa, n) = (0, 0)$ are listed in Tables 4, 5, and 6 respectively (Jiang et al., 2006). In Table 4, data are represented in three parts corresponding to $(\kappa, n) = (0, 0)$, $(\alpha, 1)$, and $(2\alpha, 2)$ respectively. From the fitting results, we can see that the contributions of θ dependence are notable comparing to those of r dependence. The velocity of the twist mode (in Table 5) as well as the polarization vectors of modes with ${}_0A_0^+$ Reps (in Table 6) are typical examples shown up an evident θ dependence.

It can be checked that all the numerically fitting expressions satisfy the symmetry requirements of Eqs (12) and (13) in section 4, where the velocities (slopes of the dispersions)

Reps	Mode	$\omega(\theta)$	$f_i(r)$
${}_0A_0^+$ R	$\vec{e}_r$ AC, 1	$f_0(r)$	$f_0(r) = \frac{1133.86}{r} - \frac{139.65}{r^3}$
	$\vec{e}_\theta$ OP, 2	$f_0(r) + f_1(r)\cos 6\theta$	$f_0(r) = 1594.00 - \frac{266.98}{r^2}$, $f_1(r) = \frac{8.65}{r^2}$
	$\vec{e}_z$ OP, 3	$f_0(r) + f_1(r)\cos 6\theta$	$f_0(r) = 1594.00 - \frac{91.81}{r^2}$,$f_1(r) = -\frac{15.68}{r^2}$, $f_2(r) = -\frac{0.68}{r^2}$
		$+f_2(r)\cos 12\theta$	
${}_0A_0^-$ Ir	$\vec{e}_r$ OP, 4	$f_0(r) + f_1(r)\cos 6\theta$	$f_0(r) = 864.81 + \frac{990.22}{r^2} - \frac{1117.30}{r^4}$, $f_1(r) = \frac{9.16}{r^2}$
${}_\alpha E_1$ R Ir	1	$f_0(r) + f_1(r)\cos 6\theta$	$f_0(r) = \frac{710.16}{r} + \frac{45.07}{r^3}$, $f_1(r) = \frac{1.99}{r^3} - \frac{31.55}{r^4}$
	2	$f_0(r) + f_1(r)\cos 6\theta$	$f_0(r) = \frac{1603.51}{r} - \frac{746.51}{r^3}$, $f_1(r) = -\frac{115.54}{r^3}$
	3	$f_0(r) + f_1(r)\cos 6\theta$	$f_0(r) = 864.84 + \frac{860.00}{r^2} - \frac{1758.70}{r^4}$, $f_1(r) = \frac{11.63}{r^2} - \frac{206.52}{r^4}$
	$\nu = \pm 1$, 4	$f_0(r) \pm f_1(r)\cos 9\theta$	$f_0(r) = 1594.13 - \frac{316.67}{r^2}$, $f_1(r) = \frac{31.92}{r^3}$
	$\nu = 0$, 4	$f_0(r) + f_1(r)\cos 6\theta$	$f_0(r) = 1594.14 - \frac{318.48}{r^2}$, $f_1(r) = \frac{7.83}{r^2} - \frac{19.03}{r^4}$
		$+f_2(r)\cos 12\theta$	$f_2(r) = \frac{2.70}{r^2} + \frac{0.60}{r^4}$
	5	$f_0(r) + f_1(r)\cos 6\theta$	$f_0(r) = 1593.97 - \frac{277.49}{r^2}$, $f_1(r) = -\frac{12.45}{r^2}$
${}_{2\alpha}E_2$ R	1	$f_0(r) + f_1(r)\cos 6\theta$	$f_0(r) = \frac{959.33}{r^2} - \frac{736.60}{r^4} + \frac{779.59}{r^5}$
		$+f_2(r)\cos 12\theta$	$f_1(r) = \frac{6.19}{r^3} + \frac{73.37}{r^4}$, $f_2(r) = -\frac{0.06}{r^3} + \frac{9.34}{r^4}$
	2	$f_0(r) + f_1(r)\cos 6\theta$	$f_0(r) = \frac{1420.21}{r} + \frac{54.52}{r^3} - \frac{1246.29}{r^5}$, $f_1(r) = \frac{204.34}{r^3}$
	3	$f_0(r) + f_1(r)\cos 6\theta$	$f_0(r) = \frac{2535.48}{r} - \frac{2426.65}{r^3}$, $f_1(r) = -\frac{412.23}{r^3}$
	4	$f_0(r) + f_1(r)\cos 6\theta$	$f_0(r) = 864.80 + \frac{486.71}{r^2} - \frac{4711.81}{r^4} + \frac{12425.61}{r^6}$
			$f_1(r) = \frac{9.89}{r^2} - \frac{524.74}{r^4}$
	5	$f_0(r) + f_1(r)\cos 6\theta$	$f_0(r) = 1594.00 - \frac{869.19}{r^2} + \frac{978.77}{r^4}$
			$f_1(r) = -\frac{16.15}{r^2} + \frac{363.41}{r^4}$
	6	$f_0(r) + f_1(r)\cos 6\theta$	$f_0(r) = 1594.01 - \frac{392.92}{r^2} - \frac{2160.15}{r^4} + \frac{5416.26}{r^6}$
			$f_1(r) = \frac{7.88}{r^2} - \frac{297.88}{r^4}$

Table 4. Frequencies (in the unit of cm^{-1}) of 15 Raman and Ir active modes as functions of r (in Å) and θ.

	Velocity(θ)	$f_i(r)$
C_{TW}	$f_0(r) + f_1(r)\cos 6\theta$	$f_0 = 13.5 - \frac{1.63}{r^2}$, $f_1 = \frac{2.38}{r^2}$
C_{LA}	$f_0(r) + f_1(r)\cos 6\theta$	$f_0 = 21.0706 + \frac{0.0055}{r} - \frac{0.6860}{r^2}$, $f_1 = \frac{0.00091}{r} - \frac{0.01679}{r^2}$
β	$f_0(r) + f_1(r)\cos 6\theta$	$f_0 = 1.3767r - 0.00142r^2 - 5.8 \times 10^{-5}r^3$, $f_1 = -\frac{0.143}{r} + \frac{0.04994}{r^3}$

Table 5. Sound velocities (in kms^{-1}) of the TW and LA modes, and β (in $10^{-6}m^2s^{-1}$) of the flexure mode as functions of r (in Å) and θ.

and frequencies are scalars while polarizations are vectors. One of the ${}_\alpha E_1$ modes in Table 4 manifests different parameter dependence for different chiral index ν, i.e. it has different expressions for $\nu = \pm 1$ and $\nu = 0$ respectively. This is still consistent with the general constrains Eqs (12) and (13).

In certain extent, the planar graphene can be viewed as the $r \to \infty$ limit of the SWCNT. As pointed out in Ref. (Jiang et al., 2006), six modes at different (κ, n) points in Table 4 evolve in this limit to the two degenerate in-plane optical modes of the graphene with approximately the same frequency limit 1594.0. While three modes with $f_0(r) \to 864.8$ approach the out-of-plane optical mode of the graphene. Moreover as shown in Table 5, the sound velocities of the two zero modes, i.e. LA and TW modes belonging to ${}_0A_0^-$, have nonzero limits with different values. Therefore, it is expected that these two modes would approach two in-plane non-degenerate acoustic modes of the graphene sheet. The situation of flexure mode

		Vector(θ)	$f_i(r)$
R_1 ($\vec{e}_r$ AC)	$u_r(A)$	$f_0(r)$	$f_0(r) = 0.7071 - \frac{0.0028}{r^2}$
	$u_\phi(A)$	$f_1(r)\sin 3\theta$	$f_1(r) = \frac{0.0518}{r} + \frac{0.0468}{r^2}$
	$u_z(A)$	$f_1(r)\cos 3\theta$	$f_1(r) = \frac{0.0517}{r} + \frac{0.0749}{r^2}$
R_2 ($\vec{e}_\phi$ OP)	$u_r(A)$	$f_1(r)\sin 3\theta$	$f_1(r) = -\frac{0.0542}{r} - \frac{0.0455}{r^2}$
	$u_\phi(A)$	$f_0(r) + f_1(r)\cos 12\theta$	$f_0(r) = 0.7056 + \frac{0.0019}{r^2}$, $f_1(r) = 0.0015 - \frac{0.003}{r^2}$
	$u_z(A)$	$f_1(r)\sin 6\theta + f_2(r)\sin 12\theta$	$f_1(r) = 0.0656 - \frac{0.0801}{r^2}$, $f_2(r) = 0.0048 - \frac{0.0112}{r^2}$
R_3 ($\vec{e}_z$ OP)	$u_r(A)$	$f_1(r)\cos 3\theta$	$f_1(r) = -\frac{0.0447}{r} - \frac{0.0417}{r^2}$
	$u_\phi(A)$	$f_1(r)\sin 6\theta + f_2(r)\sin 12\theta$	$f_1(r) = -0.0656 + \frac{0.0773}{r^2}$, $f_2(r) = -0.0048 + \frac{0.0111}{r^2}$
	$u_z(A)$	$f_0(r) + f_1(r)\cos 12\theta$	$f_0(r) = 0.7056 + \frac{0.0019}{r^2}$, $f_1(r) = 0.0015 - \frac{0.0033}{r^2}$

Table 6. Polarization vectors $\vec{u} \equiv (\vec{u}(A), \vec{u}(B))$ at $(\kappa, n) = (0, 0)$ as functions of r (in Å) and θ. Where $\vec{u}(A)$ and $\vec{u}(B)$ indicate the displacement vectors of atoms A and B in the $(0, 0)$ unit cell respectively. For the three modes in this table, $u_r(B) = u_r(A)$, $u_\phi(B) = -u_\phi(A)$, $u_z(B) = -u_z(A)$.

is complicated. The frequency of the $\vec{e}_r$ AC mode in SWCNT (Table 4) tends towards zero with its polarization vector perpendicular to the limiting sheet. This might be interpreted as a kind of precursor of the flexure mode of graphene. However, at $(\kappa, n) = \pm(\alpha, 1)$ of SWCNT, the dispersion of the two TA branch is quadratic in κ. It should be noticed that the parameterization for the coefficient β cannot be extrapolated to $r \to \infty$. This is prohibited by a kind of symmetry argument that the rod-like tube has two flexure modes with the cylindrical symmetry while the plate-like graphene sheet breaks the symmetry so as to have only one flexure mode. There is no way to cross continuously from the former to the latter.

7. References

Aizawa, T.; Souda, R.; Otani, S.; Ishizawa, Y.; Oshima, C. (1990). Bond softening in monolayer graphene fprmed on transition-metal carbide surfaces. *PHYSICAL REVIEW B*, Vol. 42, No. 18, Dec 15, 11469–11478, ISSN 1098-0121

Aizawa, T. (1991). Correction. *PHYSICAL REVIEW B*, Vol. 43, No. 14, May 15, 12060–12061, ISSN 1098-0121

Alon, O. E. (2001). Number of Raman- and infrared-active vibrations in single-walled carbon nanotubes. *PHYSICAL REVIEW B*, Vol. 63, No. 20, May 15, 201403, ISSN 1098-0121

Berger, C.; Song, Z. M.; Li, T. B.; Li, X. B.; Ogbazghi, A. Y.; Feng, R.; Dai, Z. T.; Marchenkov, A.N.; Conrad, E. H.; First, P. N.; de Heer, W. A. (2004). Ultrathin epitaxial graphite: 2D electron gas properties and a route toward graphene-based nanoelectronics. *JOURNAL OF PHYSICAL CHEMISTRY B*, VOl. 108, No. 52, December 30, 19912–19916, ISSN 1520-6106

Born, M.; & Huang, K. (1954). *Dynamical Theory of Crystal Lattices*, Oxford University Press, Oxford

Brillson, L.; Burskin, E.; Maradudin, A. A.; Stark, T. (1971). Frequencies of the long wavelength optical vibration modes of graphite, In: *The Physics of Semimetals and Narrow-Gap Semiconductors*, Carter, D.L.; & Bate, R.T., 187–193, Pergamon Press, ISBN 008016661X, Oxford, New York

Castro Neto, A. H.; Guinea, F.; Peres, N. M. R.; Novoselov, K. S.; & Geim, A. K. (2009). The electronic properties of graphene. *REVIEWS OF MODERN PHYSICS*, Vol. 81, No. 1, Januray-March, 109–154, ISSN 0034-6861

Damnjanović, M.; Milošević, I.; Vuković, T.; Sredanović, R. (1999). Full symmetry, optical activity, and potentials of single-wall and multiwall nanotubes. *PHYSICAL REVIEW B*, Vol. 60, No. 4, July 15, 2728–2739, ISSN 1098-0121

Damnjanović, M.; Vuković, T.; & Milošević, I. (2000). Modified group projectors: tight-binding method. *JOURNAL OF PHYSICS A-MATHEMATICAL AND GENERAL*, Vol. 33, No. 37, September 22, 6561–6571, ISSN 0305-4470

Das, A.; Chakraborty, B.; Sood, A. K. (2008). Raman spectroscopy of graphene on different substrates and influence of defects. *BULLETIN OF MATERIALS SCIENCE*, Vol. 31, No. 3, June, 579–584, ISSN 0250-4707

Dobardžić, E.; Milošević, I.; Nikolić, B.; Vuković, T.; & Damnjanović, M. (2003). Single-wall carbon nanotubes phonon spectra: Symmetry-based calculations. *PHYSICAL REVIEW B*, Vol. 68, No. 4, July 15, 045408, ISSN 1098-0121

Elliott, J. P. & Dawber, P. G. (1979). *Symmetry in Physics, Vol. 1*, Macmillan Press Ltd., ISBN 0333264266, London

Eyring, H.; Walter, J. & Kimball, G. E. (1949). *Quantum Chemistry*, Fifth Pringting, John Wiley and Sons Inc., New York

Ferrari, A. C.; Meyer, J. C.; Scardaci, V.; Casiraghi, C.; Lazzeri, M.; Mauri, F.; Piscanec, S.; Jiang, D.; Novoselov, K. S.; Roth, S.; Geim, A. K. (2006). Raman spectrum of graphene and graphene layers. *PHYSICAL REVIEW LETTERS*, Vol. 97, No. 18, November 3, 187401, ISSN 0031-9007

Gunlycke, D. ; Lawler, H. M.; White, C. T. (2008). Lattice vibrations in single-wall carbon nanotubes. *PHYSICAL REVIEW B*, Vol. 77, No. 1, January, 014303-1–014303-9, ISSN 1098-0121

Gupta, A.; Chen, G.; Joshi, P.; Tadigadapa, S.; Eklund, P. C. (2006). Raman scattering from high-frequency phonons in supported n-graphene layer films. *NANO LETTERS*, Vol. 6, No. 12, December 13, 2667–2673, ISSN 1530-6984

Iijima, S. (1991). Helical microtubules of graphitic carbon. *NATURE*, Vol. 354, No. 6348, November 7, 56–58, ISSN 0028-0836

Jeon, G. S.; & Mahan, G. D. (2005). Theory of infrared-active phonons in carbon nanotubes. *PHYSICAL REVIEW B*, Vol. 72, No. 15, October, 155415, ISSN 1098-0121

Jiang, J. W.; Tang, H.; Wang, B. S.; & Su, Z. B. (2006). Chiral symmetry analysis and rigid rotational invariance for the lattice dynamics of single-wall carbon nanotubes. *PHYSICAL REVIEW B*, Vol. 73, No. 23, June, 235434, ISSN 1098-0121

Jiang, J. W.; Tang, H.; Wang, B. S.; Su, Z. B. (2008)(a). Raman and infrared properties and layer dependence of the phonon dispersions in multilayered graphene. *PHYSICAL REVIEW B*, Vol.77, No. 23, June, 235421-1–235421-8, ISSN 1098-0121

Jiang, J. W.; Tang, H.; Wang, B. S.; & Su, Z. B. (2008)(b). A lattice dynamical treatment for the total potential energy of single-walled carbon nanotubes and its applications: relaxed equilibrium structure, elastic properties, and vibrational modes of ultra-narrow tubes. *JOURNAL OF PHYSICS-CONDENSED MATTER*, Vol.20, No. 4, Jan 30, 045228, ISSN 0953-8984

Madelung, O. (1978). *Introduction to Solid-State Theory*, Chap. 3, Springer-Verlag, ISBN 3540085165, Berlin

Mahan, G. D.; & Jeon, G. S. (2004). Flexure modes in carbon nanotubes *PHYSICAL REVIEW B*, Vol. 70, No. 7, August, 075405, ISSN 1098-0121

Manes, J. L.; Guinea, F.; Vozmediano, Maria A. H. (2007). Existence and topological stability of Fermi points in multilayered graphene. *PHYSICAL REVIEW B*, Vol. 75, No. 15, April, 155424-1–155424-6, ISSN 1098-0121

Mani, K. K. & Ramani, R. (1974). Lattice dynamics of graphite. *PHYSICA STATUS SOLIDI B-BASIC RESEARCH*, Vol.61, No.2, 659–668, ISSN 0370-1972

Maultzsch, J.; Reich, S.; Thomsen, C.; Requardt, H.; & Ordejon, P. (2004). Phonon dispersion in graphite. *PHYSICAL REVIEW LETTERS*, Vol. 92, No. 7, Feb 20, 075501, ISSN 0031-9007

Mohr, M.; Maultzsch, J.; Dobardzic, E.; Reich, S.; Milošević, I.; Damnjanović, M.; Bosak, A.; Krisch, M.; & Thomsen, C. (2007). Phonon dispersion of graphite by inelastic x-ray scattering. *PHYSICAL REVIEW B*, Vol. 76, No. 3, July, 035439-1–035439-7, ISSN 1098-0121

Nicklow, R.; Wakabayashi, N.; & Smith, H. G. (1972). Lattice-dynamics of pyrolytic-graphite. *PHYSICAL REVIEW B*, Vol. 5, No. 12, June 15, 4951–4962, ISSN 1098-0121

Novoselov, K. S.; Geim, A. K.; Morozov, S. V.; Jiang, D.; Zhang, Y.; Dubonos, S. V.; Grigorieva, I. V.; Firsov, A. A. (2004). Electric Field Effect in Atomically Thin Carbon Films. *SCIENCE*, Vol. 306, No. 5696, October 22, 666–669, ISSN 0036-8075 (print), 1095-9203 (online)

Painter, G.S.; & Ellis, D.E. (1970). Electronic band structure and optical properties of graphite from a variational approach. *PHYSICAL REVIEW B*, Vol. 1, No. 12, June 15, 4747–4752, ISSN 1098-0121

Partoens, B.; & Peeters, F. M. (2006). From graphene to graphite: Electronic structure around the K point. *PHYSICAL REVIEW B*, Vol. 74, No. 7, August, 075404, ISSN 1098-0121

Partoens, B.; & Peeters, F. M. (2007). Normal and Dirac fermions in graphene multilayers: Tight-binding description of the electronic structure. *PHYSICAL REVIEW B*, Vol. 75, No. 19, May, 193402, ISSN 1098-0121

Popov, V. N.; Van Doren, V. E.; & Balkanski, M. (2000). Elastic properties of single-walled carbon nanotubes. *PHYSICAL REVIEW B*, Vol. 61, No. 4, Jan 15, 3078–3084, ISSN 1098-0121

Rao, A. M.; Richter, E.; Bandow, S.; Chase, B.; Eklund, P. C.; Williams, K. A.; Fang, S.; Subbaswamy, K.R.; Menon, M.; Thess, A.; Smalley, R. E.; Dresselhaus, G.; & Dresselhaus, M. S. (1997). Diameter-selective Raman scattering from vibrational modes in carbon nanotubes. *SCIENCE* Vol. 275, No. 5297, Jan 10, 187–191, ISSN 0036-8075

Saito, R.; Dresselhaus, G.; & Dresselhaus, M. S. (1998). *Physical Properties of Carbon Nanotubes*, Imperial College Press, ISBN 1-86094-093-5, London

Tang, H.; Jiang, J. W.; Wang, B. S.; & Su, Z. B. (2009). A full spd tight-binding treatment for electronic bands of graphitic tubes. *SOLID STATE COMMUNICATIONS*, Vol. 149, No. 1–2, Jan, 82–86, ISSN 0038-1098

White, C. T.; Robertson, D. H.; Mintmire, J. W. (1993). Helical and rotational symmetries of nanoscale graphitic tubules. *PHYSICAL REVIEW B*, Vol. 47, No. 9, March, 5485–5488, ISSN 1098-0121

Ye, F.; Wang, B. S.; Su, Z. B. (2006). Symmetry restrictions in the chirality dependence of physical properties of single-wall nanotubes. *PHYSICAL REVIEW B*, Vol. 73, No. 15, April, 155424, ISSN 1098-0121

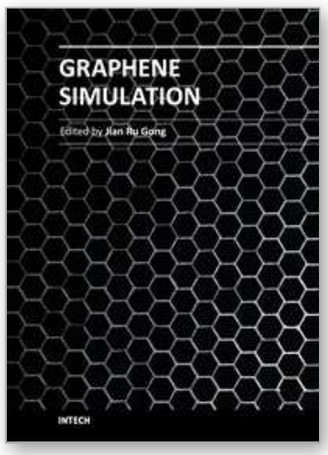

Graphene Simulation

Edited by Prof. Jian Gong

ISBN 978-953-307-556-3
Hard cover, 376 pages
Publisher InTech
Published online 01, August, 2011
Published in print edition August, 2011

Graphene, a conceptually new class of materials in condensed-matter physics, has been the interest of many theoretical studies due to the extraordinary thermal, mechanical and electrical properties for a long time. This book is a collection of the recent theoretical work on graphene from many experts, and will help readers to have a thorough and deep understanding in this fast developing field.

How to reference

In order to correctly reference this scholarly work, feel free to copy and paste the following:

Hui Tang, Bing-Shen Wang and Zhao-Bin Su (2011). Symmetry and Lattice Dynamics, Graphene Simulation, Prof. Jian Gong (Ed.), ISBN: 978-953-307-556-3, InTech, Available from: http://www.intechopen.com/books/graphene-simulation/symmetry-and-lattice-dynamics

INTECH
open science | open minds

InTech Europe
University Campus STeP Ri
Slavka Krautzeka 83/A
51000 Rijeka, Croatia
Phone: +385 (51) 770 447
Fax: +385 (51) 686 166
www.intechopen.com

InTech China
Unit 405, Office Block, Hotel Equatorial Shanghai
No.65, Yan An Road (West), Shanghai, 200040, China
中国上海市延安西路65号上海国际贵都大饭店办公楼405单元
Phone: +86-21-62489820
Fax: +86-21-62489821

© 2011 The Author(s). Licensee IntechOpen. This chapter is distributed under the terms of the Creative Commons Attribution-NonCommercial-ShareAlike-3.0 License, which permits use, distribution and reproduction for non-commercial purposes, provided the original is properly cited and derivative works building on this content are distributed under the same license.

IntechOpen

IntechOpen